J. Fluid Mech. (1987), *vol.* 179, *pp.* 407–438
Printed in Great Britain

Transition of transient vertical natural-convection flows in water

By YOGENDRA JOSHI
Department of Mechanical Engineering, Naval Postgraduate School, Monterey, CA 93943, USA

AND BENJAMIN GEBHART
Department of Mechanical Engineering and Applied Mechanics, University of Pennsylvania, Philadelphia, PA 19104, USA

(Received 6 June 1986)

Experimental results and interpretations are given for transient natural convection adjacent to a suddenly heated flat vertical surface in quiescent water. The 1.24 m high surface resulted in laminar, transition and turbulent regimes downstream, in transients and in steady state, over a wide range of surface-energy input rates. Flows were visualized and velocity and temperature measurements made at various downstream locations, after imposing a uniform internal-energy generation rate within the very thin surface. Upflow development from quiescence to steady state was found to depend strongly on the downstream location x and imposed input heat flux. Laminar flow persisted into steady state, for short downstream distances. Further downstream, the flow became turbulent during the transient. Relaminarization at later time occurred only for lower flux inputs. Local measurements across the fluid layer show that the transient disturbances close to the leading edge of the surface are confined to within the final steady boundary layer. Downstream, they extend much further into the ambient. First disturbances always arose before the leading-edge-effect propagation estimates. The trend of data was in agreement with theory for a non-dimensional time $\tau < 85$. For larger τ, turbulence instead terminated the one-dimensional transport regime simultaneously, at all downstream locations. This single value of τ also amounts to a single value of the non-dimensional thermal energy of the flow, $E_{TT} = 19.7$. Disturbance frequency data early in the transient suggest the presence of a strongly selective amplification mechanism, very similar to that found in steady flows. The non-dimensional times at which local steady state was achieved were best correlated by a Fourier number, over a wide range of energy input conditions. Turbulence arising during the transient enhances the thermal transport significantly. Local convection coefficients then were found to be as much as 40 % higher than the eventual steady values.

1. Introduction

Buoyancy-induced flow transients are important in many environmental and technological processes. These applications include cooling of a reactor core in a power or pump failure and the startup and shutdown of equipment. The possibility of encountering extreme states is frequently of concern in such circumstances. Similar considerations arise in assemblies of microelectronic devices, when natural convection is the mode of cooling.

1.1. *Previous analysis*

The earliest study of transients adjacent to vertical surfaces appears to be that of Illingworth (1950). It was shown that early transient response to an impulsive and uniform change in the surface boundary condition is one-dimensional outward. Then, heat transfer from the surface to the fluid is purely through conduction. This results in a transient temperature field which is invariant downstream along the surface. This temperature field produces a one-dimensional buoyancy force and resulting velocity distribution. Closed-form solutions were obtained for the transient velocity $u(y,\tau)$ and temperature $t(y,\tau)$ distributions. One-dimensional solutions were also obtained by Schetz & Eichorn (1962) and Menold & Yang (1962) for many different surface conditions. On the other hand, Yang (1960) applied non-uniform transient surface conditions, and obtained similarity solutions.

In practice, for a finite surface, one-dimensional response persists only for a short time. Pressure and convective effects quickly result in the development of entrainment, up from the leading edge of the surface.

The flow response eventually establishes steady transport. Siegel (1958), using the method of characteristics, obtained time estimates both for the end of one-dimensional processes and the establishment of steady laminar boundary-layer flow. The Kármán–Pohlhausen integral technique gave a set of coupled hyperbolic equations for the local boundary-layer thickness and the characteristic velocity.

Goldstein & Briggs (1964) suggested a method of predicting arrival time of the leading-edge effect, or disturbance, at a given downstream location x_p. This penetration distance was maximized over y, at a given τ, to arrive at the following expression for the penetration distance:

$$x_p(\tau) = \max\left\{\int_0^\tau u(y,\tau')\,d\tau'\right\}. \tag{1}$$

1.2. *Effects of surface thermal capacity*

The above analyses, with the exception of that of Goldstein & Briggs (1964), determined the transport resulting from specified changes in either the surface temperature or heat-flux levels. In practice, these conditions are not generally realistic. When any actual surface is heated suddenly, for example, by passing an electric current through it, part of the thermal-energy input rate is stored in the surface material. The rest is transferred to the fluid. The resulting energy balance at the surface, at $y = 0$, is given by

$$q''_\infty = c''\frac{\partial t}{\partial \tau} - k\frac{\partial t}{\partial y}. \tag{2}$$

Here q''_∞ is the imposed rate of energy generation in the material per unit surface area. The first term on the right is the rate of changing energy storage in a surface of relatively large thermal conductivity. The second term is the heat conducted away to the adjacent fluid. At steady state, the storage term has become zero and the input q''_∞ becomes the uniform surface heat flux to the fluid.

The fraction of the total transient time for which a one-dimensional process persists in the fluid was found by Gebhart (1961) to depend on ratio of the thermal capacity of the surface, c'', to that of the fluid. Suitable non-dimensionalization of (2), as by Sammakia & Gebhart (1978), yields the following relevant parameter:

$$Q^* = c''\left[\frac{g\beta q''_\infty \nu^2}{k^5}\right]^{\frac{1}{4}}. \tag{3}$$

If Q^* is very large, the one-dimensional conduction process in the fluid lasts for a relatively short time. The leading-edge effect propagates downstream early during the transient. Thereafter, the subsequent approach to the eventual steady state is a quasi-static process. Surfaces with very small values of Q^* have a longer duration of the initial one-dimensional response, as with thin surfaces in water. For a detailed discussion of these regimes, see Gebhart (1971). The details of the initial integral analysis by Gebhart (1961) are also summarized there.

1.3. *Other studies*

The transient boundary-layer equations have been numerically integrated for a step increase in the surface temperature of a vertical surface by Sugawara & Michiyoshi (1951), Hellums & Churchill (1961) and Ingham (1978*a*, *b*). Callahan & Marner (1976) considered transient mass transfer. Transients following a sudden internal-energy generation rate within a vertical surface were also studied, by Sammakia & Gebhart (1978, 1981).

A recent and extensive analysis of transients, following a uniform step increase of the surface temperature, is given by Brown & Riley (1973). The entire transient is divided into three distinct response regimes in time. The first corresponds to the initial one-dimensional purely diffusive transport. At a particular value of the time variable, departures from the one-dimensional solution arise as an essential singularity. Solutions in the neighbourhood of this time are determined only within a constant. This arises from the absence of boundary conditions at the upstream leading edge. The calculation of leading-edge penetration rate is again based on the general assumption that the fastest leading-edge signal travels at the local instantaneous maximum velocity in the boundary layer. However, the resulting expression for distance is

$$x_{\mathrm{p}}(\tau) = \int_0^{\tau} \max\left[u(y, \tau')\right] \mathrm{d}\tau'. \tag{4}$$

This formulation yields propagation rates only slightly faster than (1).

The third stage of the transient is taken as a perturbation, backward in time, from the eventual steady state. Solutions are again found only to within a constant. The approach to the steady state was found to be exponential in time. This is also characteristic of many impulsively started forced flows.

The finite-difference analysis of Ingham (1978*a*) indicates that the small- and large-time solutions of Brown & Riley (1973) are not properly matched through finite-difference schemes such as the one used by Hellums & Churchill (1961). Ingham (1978*b*), has shown that other techniques to integrate the equations numerically, to estimate the two undetermined constants in the analysis of Brown & Riley (1973), have not been successful.

1.4. *Previous measurements*

The measurements to date, of natural-convection transients adjacent to vertical surfaces, are summarized in table 1. Those by Klei (1957), Martin (1961), Lurie & Johnson (1962), Gebhart & Adams (1963) and Gebhart, Dring & Polymeropoulos (1967) have considered average surface transport during the transient. Goldstein (1959) studied the local surface transport and the transient development of the thermal boundary layer, in air and water. Rajan & Picot (1971) report local heat-transfer coefficients in four different fluids.

Investigator(s)	Fluid	Gr^*	Gr	Q^*	ΔT(°C)	Height of surface (cm)	Experimental technique
Klei† (1957)	Air	—	7.9 to 12×10^4	12.6 to 15.4	50.6 to 110.6	2.5	Thermocouple measurements
Goldstein (1959)	Water	1.8 to 4.8×10^8	3.4 to 7.8×10^6	0.06 to 0.08	0.3 to 0.6	16.5	Interferometry
	Air	4.3 to 7.7×10^8	1.3 to 1.9×10^7	20.1 to 23.2	5.9 to 21.2	20.3	
Martin (1961)	Water	1.3 to 23×10^7	4.3 to 34×10^5	0.4 to 0.8	6.7 to 52.8	2.5	Resistance
	Water	2.8 to 21×10^9	5.3 to 23×10^6	0.3 to 0.5	5.3 to 23.1	6.4	thermometry
	Water	1.4 to 6.5×10^9	1.9 to 5.9×10^7	0.3 to 0.5	6.9 to 21.4	8.9	
Lurie & Johnson (1962)	Water	1.8×10^{11}	9.2×10^8	1.2	63.3	7.6	Resistance thermometry
Gebhart & Adams (1963)	Air	7.7×10^6	5.0×10^5	282.3	129.4	3.8	Infra-red
	Air	4.5×10^7	2.2×10^6	24.8	125.0	6.4	detector
	Air	8.7×10^7	4.6×10^6	7.3	110.0	7.6	
Gebhart, Dring & Polymeropoulos (1967)	Pressurized nitrogen	2.4 to 510×10^9	5.4 to 400×10^7	2.3 to 12.8	2.7 to 41.9	18.4	Interferometry
Mollendorf & Gebhart (1970)	Pressurized nitrogen	1.8 to 61×10^{12}	9.1 to 120×10^9	2.7 to 5.1	5.6 to 27.3	50.2	Interferometry
Rajan & Picot (1971)	$Pr \sim 6$–10^6	4.1×10^1 to 2.4×10^{10}	—	—	~3	25.4	Thermocouple measurements
Mahajan & Gebhart (1978)	Pressurized nitrogen	2.5 to 150×10^9	—	2.9 to 32.3	2 to 80	38.5	Hot-wire and thermocouple measurements
Sammakia, Gebhart & Qureshi (1980)	Air	3.7 to 69×10^{11}	—	284	~4.1 to 95.9	130.5	Thermocouple measurements
Sammakia, Gebhart & Qureshi (1982)	Water	6.7×10^5 to 12×10^8	—	1.2 to 2.0	—	130.5	Thermocouple measurements
Present investigation	Water	2.7×10^8 to 10^{13}	—	0.86 to 1.14	~2 to 8.7	124.0	Hot-film and thermocouple measurements and flow visualization

† Based on data reported by Siegel (1958)

TABLE 1. Summary of experimental studies of natural-convection transients adjacent to a vertical surface

Using the interferometric data of Gebhart *et al.* (1967), Gebhart & Dring (1967) obtained times for the termination of one-dimensional processes. These were found to be 15–20 % earlier than the predictions in (1). The difference was summarized to be due to pressure effects neglected in the one-dimensional analysis. Even faster propagation rates in pressurized nitrogen, were found by Mahajan & Gebhart (1978), using very fine local sensors.

Sammakia, Gebhart & Qureshi (1980) measured transient local surface-temperature response in air, with appreciable radiation effects. The same configuration was considered by Sammakia, Gebhart & Qureshi (1982), to obtain local surface and fluid temperature data in laminar transients in water.

Mollendorf & Gebhart (1970) studied more vigorous transients. These began as laminar flow but were primarily turbulent in steady state. Using a Mach–Zehnder interferometer, convection layers were observed in nitrogen gas adjacent to a vertical foil, in the downstream region 25.4 to 45.7 cm. The initially one-dimensional laminar flow response became turbulent, soon after the arrival of leading-edge disturbances. Two heat input levels were studied. At the lower value, $q''_\infty = 92.8$ W/m^2, the flow relaminarized. For $q''_\infty = 849.7$ W/m^2, the flow remained turbulent after transition. No observations were reported for $x < 25.4$ cm. Also the interferometric data did not give information about flow features during the transient, such as entrainment development.

The present study investigated in detail the transient transport development adjacent to a tall vertical surface. Regions of laminar, transition and turbulent flow exist in steady state. Their time evolution, starting from quiescence, was studied experimentally. Water was chosen as the fluid medium for two reasons. First, flow velocities in water are conveniently an order-of-magnitude smaller than in air, for comparable heating conditions. This results in fairly long transient times, from 2–4 min. Secondly, a simple flow visualization could be achieved, using suspended particles.

2. Experimental apparatus and procedure

The transient flow was generated adjacent to a vertical surface assembly 1.24 m high and 0.37 m wide. This assembly consists of two 0.038 mm thick foils of Inconel 600, separated by layers of fabric impregnated with a thermosetting resin. Copper–constantan thermocouples of 0.05 mm diameter were placed within layers of the fabric. The entire assembly was bonded in a steam press at approximately 175 °C, under 28 atm pressure. The final thickness of the resulting surface was approximately 0.28 mm, or 11 mils. This very thin configuration had very low thermal capacity. This assured that the embedded thermocouple transient responses were close to that of the surface. Also, the very small amount of thermal-energy storage in this thin surface assembly resulted in a surface-temperature response close to that of an element having zero relative thermal capacity. These detailed considerations are included in Joshi (1984).

Figure 1 is a schematic sketch of the experimental arrangement. The stainless tank was 1.83 m × 0.622 m × 1.83 m high, with glass windows for flow visualization. Sudden heating was imposed along the vertical surface, on both sides, by applying an electric current through the Inconel surface layers. The surrounding water was maintained pure and free of ionic contamination, with a water treatment system. This consisted of an organic filter, two de-ionizer cartridges and a 0.5 μm filter in series. A resistivity level of about 1 MΩ cm was thereby maintained during the measure-

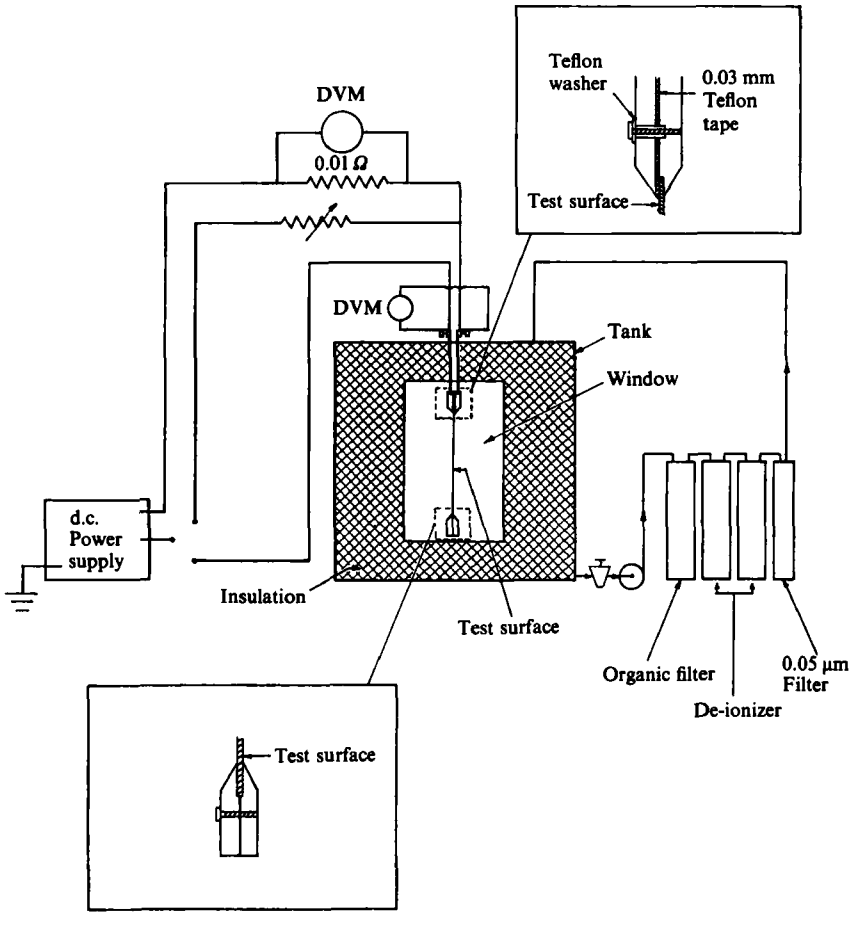

FIGURE 1. Schematic sketch of the experimental apparatus.

ments. Contamination at the free surface, through contact with atmospheric air, was minimized by floating Teflon-coated rafts.

The electrical circuit consisted of a 0–110 V and 0–100 A d.c. power supply, connected in series with the test surface, a precision resistor and a variable resistance. During a typical test, the power supply was warmed for about 30 min on an auxiliary parallel resistance, approximately the same as that of the surface. The transient was begun by switching from the auxiliary resistance to the test circuit. The switching time was negligible compared to that of the total transient. The input closely resembled a step in the surface-energy generation rate. The voltage drop across the surface was measured by a DVM. A second DVM was used to measure the voltage drop across the 0.01 Ω series resistor. These measurements determined the thermal input rate to the surface element to very high accuracy.

For the visualization of the flow response at various heating inputs, a 3 mW helium–neon laser beam was spread into a vertical thin layer or curtain of light. A plane mirror and cylindrical lens combination was used, see Carey & Gebhart (1981). The layer of light was downward, at mid-span of the surface. Finely ground particles of neutrally buoyant Pliolite were suspended in the water. The scattered laser light marks the motion of the particles on Kodak 400 I.S.O. Tri-X film. A motor-driven

camera and an intervalometer allowed flexible and close control of both the exposure time and the interval between successive frames.

After the visualization studies were complete, the tank water was recirculated through the purification system, in preparation for the sensor measurement programme. The Pliolite particles were completely removed before the sensors were introduced, since any particulate matter might affect their response.

Measurements of temperature response in the transient convective fluid layer were by a 0.076 mm diameter copper–constantan thermocouple, referenced to an ice-water bath. Its response time was about 30 m s. This is negligible compared both to the total transient time and to the periodic variations, at about 0.5 Hz, which arose in this study. The thermocouple leads were parallel to the surface for about 3 mm from the junction, to minimize lead conduction away from the junction.

Velocity measurements were with a constant-temperature anemometer system, using a calibrated fibre film probe of 90 μm diameter and active length of 1.25 mm. A protective quartz coating makes it suitable for use in water. It was calibrated in an isothermal steady flow in the range 0–4 cm/s, using the procedure described by Shaukatullah (1977). The calibration was in terms of $u = f(E - E_0)$ where u is the velocity and $(E - E_0)$ is the incremental anemometer voltage output, above zero velocity. A fifth-order-polynomial fit of the data determined the function $f(E - E_0)$. Various overheat ratios were used, to compensate for temperature variations in the fluid region. The response time of the film probe was about 30 μs.

The film and the thermocouple probes were at the same vertical height. A manual traversing mechanism, with a least count of 0.025 mm, was used to traverse the probe assembly normal to the surface. The surface was located as it closed an electric circuit between a contact on the probe assembly and the surface. The relative position of the thermocouple and hot film were, in turn, accurately determined from enlarged photographs of the holder assembly.

A digital data acquisition system automatically stored all measurements on tape. This system consists of a scanner, DVM and microcomputer. The fluid sensor measurements required two different ranges, microvolt for the thermocouple and volts for the hot film. Autoranging was used at a scan rate of about 10 channels per second.

3. Flow visualization

The visualizations of the flow evolution, in ambient water at $t_\infty \approx 20$ °C, are discussed first, to clarify the salient flow features of transient response. The sensor data given in later sections support these observations and give additional critical detailed information. The flow was visualized for heat-flux inputs q''_∞ from 92 to 1873 W/m². Because of the tall surface, two visualization runs were necessary for each heating condition, one for the lower and the other the upper part of the region. Flow evolution was found to be markedly different across the wide range of energy input and along the surface height.

3.1. *Transient response at low thermal input*

Figure 2 (*a*, *b*) shows the transient sequence of flow development, for $q''_\infty = 92$ W/m². This very low flux level results in steady laminar flow over most of the surface. It is a reference for comparison with flows at higher heating rates. Figure 2 (*a*) shows the response adjacent to the lower part of the surface, $x = 0$ to 53 cm. Figure 2 (*b*) is for $x = 52$ to 105 cm.

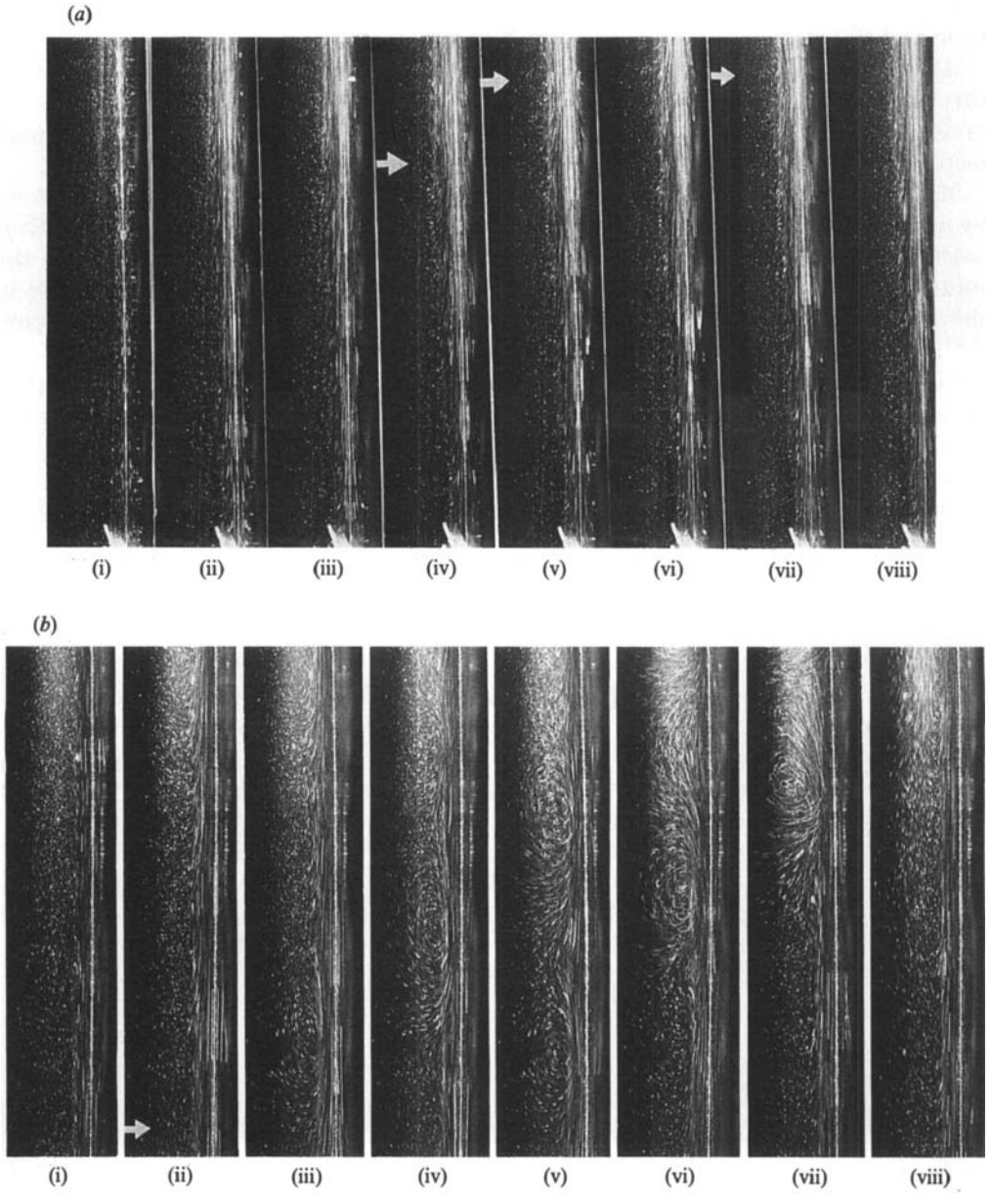

FIGURE 2. Flow visualization for low-thermal-input transient. (*a*) Lower part of the surface; $0 < x < 53$ cm, $q''_\infty = 92$ W/m^2. Exposure durations in s are (i) 22–32, (ii) 77–87, (iii) 110–120, (iv) 143–153, (v) 154–164, (vi) 165–175, (vii) 176–186, (viii) 242–252. (*b*) Upper part of the surface; $52 < x < 105$ cm, $q''_\infty = 92$ W/m^2. Exposure durations in s are (i) 73–83, (ii) 161–171, (iii) 172–182, (iv) 183–193, (v) 194–204, (vi) 216–226, (vii) 260–270, (viii) 458–468.

Immediately after the heating is imposed, in (i), flow is one-dimensional over the whole surface. Entrainment development has already started in (ii). At 120 s, in (iii), the entrainment has already developed along the entire length seen, to $x = 53$ cm. In (iv), a counterclockwise vortex has appeared, at the arrow, at about $x = 35$ cm, in the outside of the flow layer. It has moved up in (v) and out of the field by (vi).

A second vortex forms in (vii) and moves downstream. In (viii), at about 250 s, flow has achieved steady state over the entire length seen in figure 2(*a*).

In the upper part of this flow, in figure 2(*b*), at short times in (i), the flow is also one-dimensional. In (ii), entrainment has now developed along the whole upper length and a vortex has appeared adjacent to the lower part of the surface at the location of the arrow. In (iii), a downstream sequence of initially equispaced vortices has appeared. The 'eye' of each vortex is at the outer edge of the buoyant fluid layer. They have moved up in (iv). The flow inside these vortices becomes irregular and locally turbulent, as seen downstream of the second vortex in (v). For later times, in (vi) and (vii), the turbulent flow is swept progressively downstream. The final steady profile in (viii) shows a laminar flow pattern for $x < 92$ cm.

This flow response is summarized as follows. At short time it is one-dimensional. Entrainment development then terminates this phase as it moves downstream. This occurs early in any transient. The entrainment propagation rate is compared with calculations in §5: the trends agree. After entrainment has developed near the top of the surface, counterclockwise vortices first appear. Later, additional laminar equispaced vortices appear above $x = 33$ cm. These are convected downstream. They then merge and degenerate into turbulence. This turbulence is swept downstream. It is followed by the re-establishment of laminar flow, progressively downstream, into a laminar steady flow.

This kind of one-dimensional initial development has been seen in all previous experimental studies. However, none of those studies have reported vortex formation during the transient. This may be due to the short test-surface height in those studies. With a relatively tall surface, Mollendorf & Gebhart (1970) had found sinusoidal disturbances. They amplified and caused turbulence in air. They eventually relaminarized at low thermal inputs. Since the visualizations were interferograms, no surmises may be made about other flow details during the transient.

3.2. *Transient response at higher heating rates*

At higher inputs, the first difference was that disturbances appeared in the one-dimensional flow, even before the leading-edge, or entrainment, penetration from upstream. These disturbances amplified and caused local transition to turbulence. Relaminarization occurred later, but only adjacent to the lower part of the surface. This same sequence of events was seen for q''_∞ over the range from 585 to 1874 W/m^2. Therefore, only the visualizations for the highest heating condition, $q''_\infty =$ 1874 W/m^2, are discussed here.

Figure 3(*a*) shows flow development for $x < 46$ cm. At short times, the flow response is similar to that at 92 W/m^2. The one-dimensional flow in (i) is followed by entrainment propagation in (ii) and (iii). Entrainment development is complete by (iv) and disturbances are forming downstream, near the top of the picture. However, these disturbances are not distinct vortices, as are those in figure 2. These amplify in (v) and the flow appears to have become turbulent for $x > 33$ cm. For later times, in (vi) and (vii), the flow relaminarizes progressively downstream. The resulting steady flow is seen in (viii).

The flow evolution adjacent to the upper part of the surface, in figure 3(*b*), is one-dimensional in (i). In (ii), small disturbances are seen, within this one-dimensional flow. No entrainment has arisen. Entrainment has developed to $x \leqslant 73$ cm, in (iii). The disturbances first seen in (ii) have amplified downstream along the entire surface, for $52 < x < 106$ cm. These disturbances appear initially sinusoidal in (iii). This flow is further distorted in (iv) and becomes turbulent in (v). Later, in (vi), the flow

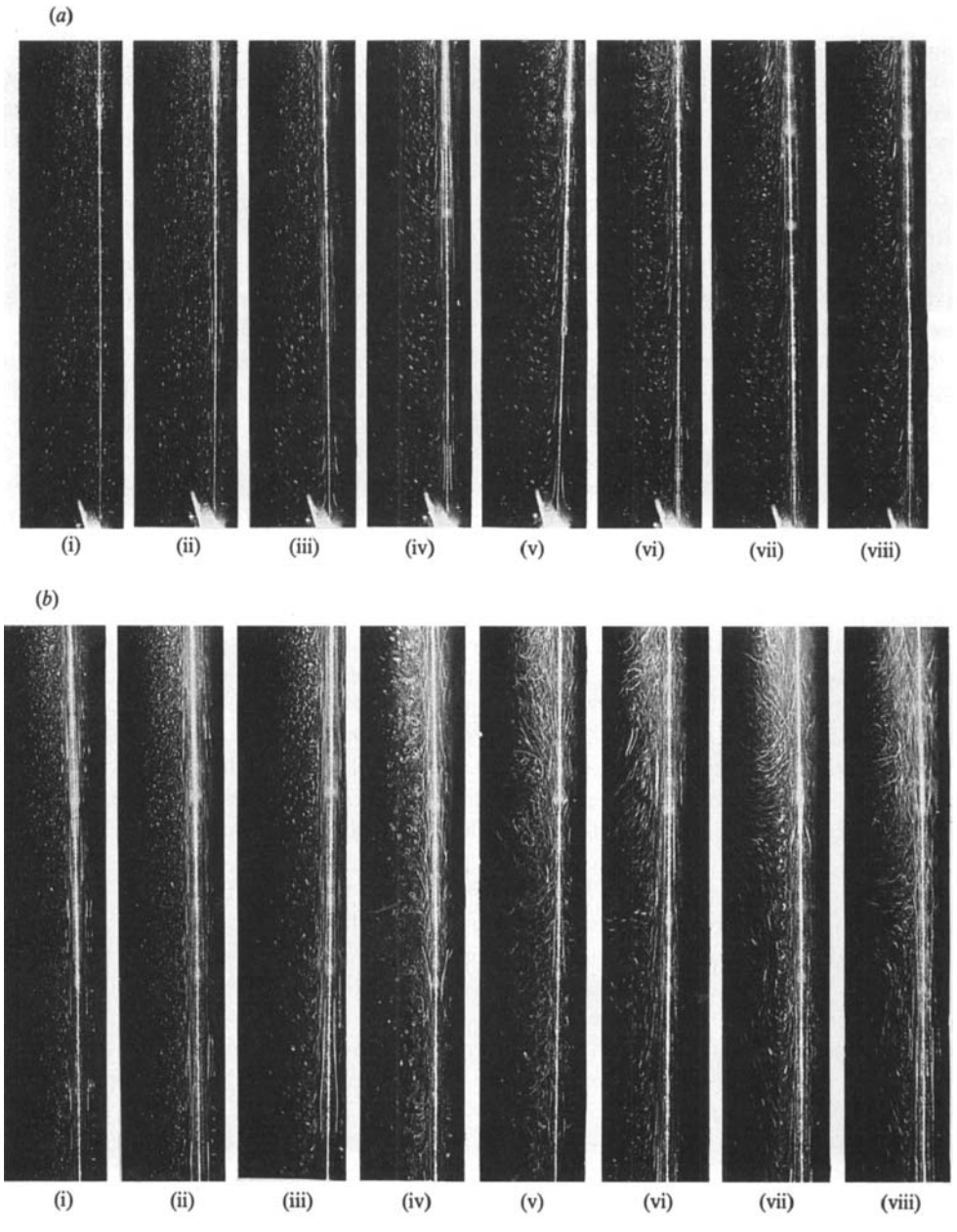

FIGURE 3. Flow visualization for high-thermal-input transient. (*a*) Lower part of the surface; $0 < x < 45.9$ cm, $q''_\infty = 1874$ W/m^2. Exposure durations in s are (i) 0–8, (ii) 8.5–16.5, (iii) 17–25, (iv) 25.5–33.5, (v) 42.5–50.5, (vi) 51–59, (vii) 68–76, (viii) 102–110. (*b*) Upper part of the surface; $51.9 < x < 106.0$ cm, $q''_\infty = 1874$ W/m^2. Exposure durations in s are (i) 18.5–26.5, (ii) 27–35, (iii) 35.5–43.5, (iv) 44–52, (v) 52.5–60.5, (vi) 180–188, (vii) 248–256, (viii) 265–273.

becomes more ordered in the lower part, as steady state is achieved. Subsequent photographs showed intermittent turbulent bursts in the region $52 < x < 65$ cm. Such bursts are characteristic of steady flow transition to turbulence, see Jaluria & Gebhart (1974). In the burst seen in (vii), near the bottom of the picture, the streaks

are irregular. A more orderly pattern is seen in (viii), after its passage. Flow downstream of $x = 76$ cm was always turbulent after 52 s.

In summary, for the entire surface, early one-dimensional response is followed by entrainment development downstream from the leading edge. However, disturbances now arise, in the upper region, even before entrainment has developed there. These disturbances amplify and the flow becomes turbulent for $x > 30$ cm. Later, the flow relaminarizes adjacent to the lower part, as transition and developed turbulence are established further downstream.

For the heating condition of $q''_\infty = 848.7$ W/m^2, in the study by Mollendorf & Gebhart (1970) in a gas, turbulence occurred only after the passage of the leading-edge effect and the attendant disturbances. These visualizations in water clearly indicate a very different mechanism. Disturbances arise in the one-dimensional flow response, well before the leading-edge effect arrives. This is, instead, the result of a purely one-dimensional instability mechanism.

These visualizations show several complex aspects of transient flow response and evolution. Based on the whole body of flow visualizations, and on the local sensor data presented in later sections, a flow-regime diagram, figure 4, was constructed. It summarizes flow development in the range $10^8 \leqslant Gr_x^* \leqslant 10^{13}$ and is discussed next.

4. Flow-regime diagram

All of the regimes seen in the visualizations are represented in figure 4. There were two kinds of processes, transients and the eventual steady state. The area in figure 4 representing the transients is at the lower left. It terminates at the heavy solid diagonal line. This indicates the completion of transient response in all of the experiments. Each particular transient response at a given q''_∞ and x is a vertical line in that region.

The eventual steady-state regimes downstream along the surface are shown by the region in the upper-right portion of figure 4. The regimes are laminar, followed by transition and turbulence. These regions are separated by the transition parameters E and Q_{ET}.

4.1. *Transient flow regimes*

The region of transients, in the lower-left triangular area of the diagram, is in terms of Fo and Gr_x^*, where $Fo = \alpha\bar{\tau}/x^2$, with $\bar{\tau}$ the physical time into the transient, and $Gr_x^* = g\beta q''_\infty x^4/k\nu^2$. The upper steady-state boundary reached by these flows was found in these measurements to be about $Fo = 0.596\, Gr_x^{*-0.35}$, as given in §7.

At any given combination of heat-flux level q''_∞ and downstream location x, the transient proceeds in time along a vertical path of increasing Fo. An example is shown, at $Gr_x^* = 10^9$. At small Fo, the flow is one-dimensional, in regime I. Later in regime II, the leading-edge effect arrives, at this x. A two-dimensional laminar flow develops to begin region III. In region IV, any disturbances that have arisen have damped out, to result in a steady laminar flow, beyond the bounding line. This is at about $Fo = 4 \times 10^{-4}$. At the low heating rate, 92 W/m^2, counterclockwise vortices were seen in region IV, just before steady state was reached.

Had $q''_\infty x^4$ resulted in a value of Gr_x^* greater than about 10^{11}, a different transient sequence would have resulted, as seen in the lower region on the right. From $Gr_x^* = 10^{11}$, up to about 2×10^{11}, the more vigorous transient would have gone directly from entrainment development, in region II, into a brief period of disturbance

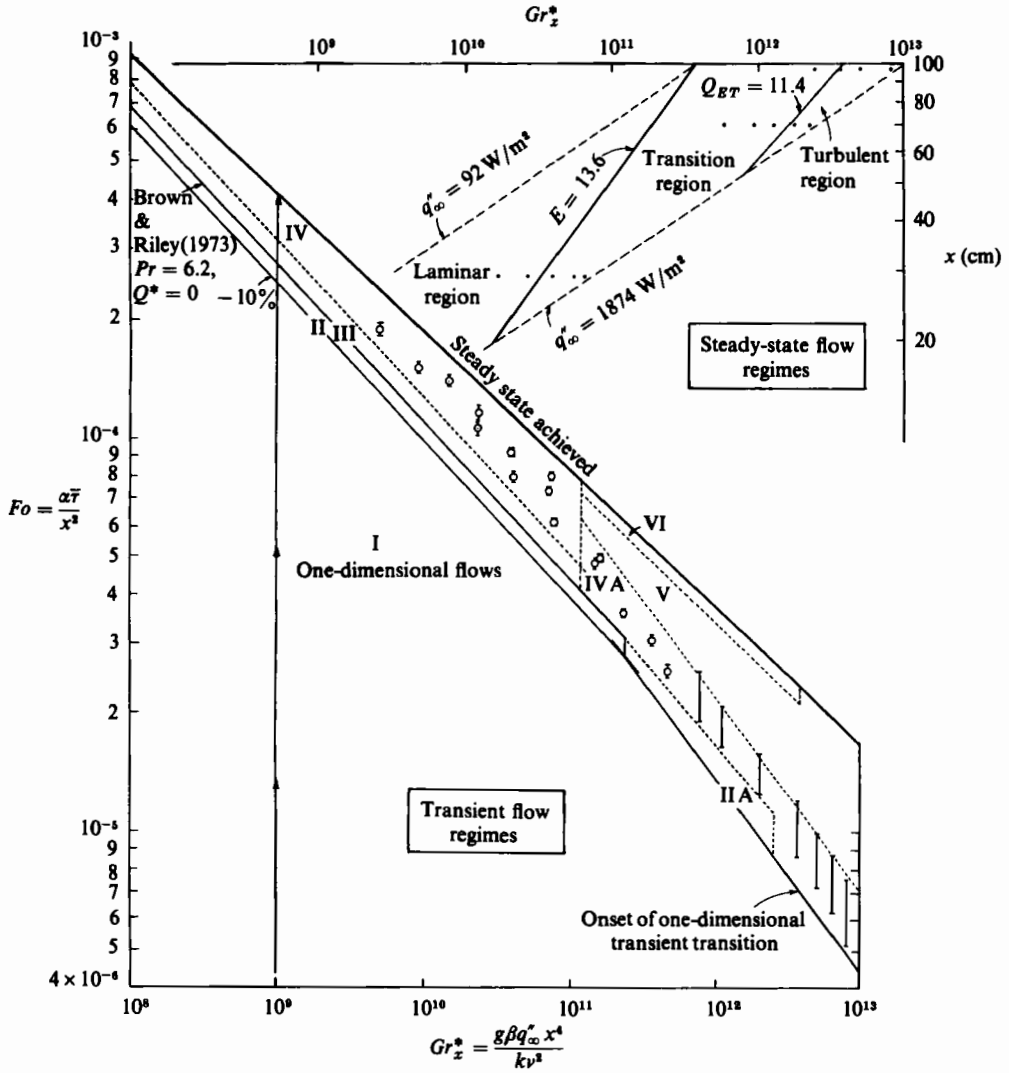

FIGURE 4. Regime diagrams for the transient and for the steady flows. The transient regimes identified are (I) laminar one-dimensional, (II) entrainment development in laminar flow, (IIA) entrainment development following onset of one-dimensional transient transition, (III) laminar two-dimensional flow, (IV) damping disturbances, (IVA) transient disturbance growth, (V) turbulent flow and (VI) partial relaminarization. The data shown are: I, sensor measurements; $\dot{Q}$, times when vortices were observed; ·, steady sensor data.

growth. This mechanism causes transition, during the time interval in region IVA. Later, in time interval V, the flow is turbulent. Finally, in the brief time interval, in VI, the flow has partially relaminarized by the time steady state is reached.

In the additional higher range, up to about $Gr_x^* = 2.5 \times 10^{12}$, the entrainment effect arrives in region IIA, that is, after the onset of one-dimensional transient transition. Above $Gr_x^* = 2.5 \times 10^{12}$, the one-dimensional flow disturbances grow in region IVA to cause turbulence in region V, even before the entrainment effect arrives. Thus, the one-dimensional laminar regime is terminated directly into one-dimensional transient transition.

The above diversity of transient response mechanisms, over the range of about $Gr_x^* = 10^8$ to 10^{13}, indicates the interplay of many simultaneous and competing effects. The initial one-dimensional temperature and flow fields inevitably generate a downstream-propagating leading-edge effect. For weaker flows, that is, at smaller $q''_\infty x^4$, this effect produces two-dimensional developing flow. A competing mechanism generates disturbances. These are damped into steady state. However, at larger $q''_\infty x^4$, appreciable disturbances arise earlier in the transient sequence. At the largest values of Gr_x^*, these disturbances even appear in the initial one-dimensional laminar phase, to cause transition to full turbulence. Thus, the interplay of basic effects changes between two extremes across this range. The locations of some of the measurement and visualization evidence from which the transient regimes on figure 4 were postulated are shown by the symbols defined in the caption.

4.2. *Regimes of steady flow*

The triangular region at the upper right in figure 4, above the line at which steady state is achieved, represents steady flows. The laminar, transition and turbulent flow regions are shown, for example, as they would arise as a steady downstream sequence in a flow adjacent to a tall vertical surface with a uniform surface flux q''_∞. Two such paths downstream are shown as the dashed lines in that region. These paths correspond to $q''_\infty = 92$ and $q''_\infty = 1874$ W/m^2, the lower and upper limits in these experiments. All the steady-state data taken are, therefore, contained within the region bounded by these two parallel lines.

The fourteen data points in figure 4, at $x = 30$, 70 and 96.8 cm, are the conditions at which sensor measurements were made. Over the heat-flux range of the experiments, the steady flow regime was laminar, for $Gr_x^* < 1.5 \times 10^{10}$. Transition occurs at higher Gr_x^*, depending on the level of q''_∞.

The experiments of Jaluria & Gebhart (1974) determined the conditions for the beginning of transition in such steady flows in water. The measure of its beginning was a decrease of the velocity or temperature trends downstream, from the laminar growth rates. The data did not correlate with Gr_x^* alone. There was an additional q''_∞ (or x) dependence. The following parameter correlated the beginning of transition:

$$E = G^* \left(\frac{\nu^2}{gx^3}\right)^{\frac{2}{15}} = 5(\tfrac{1}{5}Gr_x^*)^{\frac{1}{5}} \left(\frac{\nu^2}{gx^3}\right)^{\frac{2}{15}}. \tag{5}$$

$E = 13.6$ and 15.2 were suggested for velocity and thermal transition, respectively.

Mahajan & Gebhart (1979) further refined the parameters, in particular the role of kinematic viscosity, with experiments in pressurized gas. The end of transition, signalled by no further appreciable change in the intermittency distributions, was given by $Q_{ET} = 11.4$, where

$$Q_{ET} = 11.4 = G^* \left(\frac{\nu^2}{gx^3}\right)^{\frac{1}{6}} Pr^{\frac{1}{3}}. \tag{6}$$

The two limits, (5) and (6) on figure 4, define the three flow regimes. The experimental conditions and steady transition parameters, for the measurements reported here, are collected in table 2. These data cover a wide range, $E = 12.1$ to 25.8. They span from laminar through transition to early turbulence in steady state, as seen in figure 4.

Figure 4 is a complete description of the transient and steady flow regimes for the range of conditions studied in water. Local sensor responses are discussed in the next section. Then, the transition and turbulence arising during the transient, which have

Run	x (cm)	η_v	η_t	q''_∞ (W/m^2)	Q^*	G^*	E	Q_{ET}
1	29	0.65	0.47	588	0.86	401	12.1	7.3
2	29	0.71	0.52	843	0.94	440	13.1	7.9
3	29	0.75	0.56	1141	1.01	477	14.1	8.5
4	29	0.77	0.60	1503	1.08	508	15.0	9.0
5	29	1.23	1.00	1503	1.08	508	15.0	9.0
6	29	1.62	1.40	1503	1.08	508	15.0	9.0
7	29	2.84	2.61	1503	1.08	508	15.0	9.0
8	29	4.19	4.07	1503	1.08	508	15.0	9.0
9	29	0.85	0.62	1874	1.14	527	15.8	9.4
10	70	0.57	0.42	588	0.86	816	17.2	9.6
11	70	0.63	0.46	843	0.94	894	18.7	10.3
12	70	0.67	0.49	1141	1.01	956	20.1	11.0
13	70	0.71	0.52	1503	1.08	1020	21.3	11.6
14	70	1.45	1.26	1503	1.08	1020	21.3	11.6
15	70	2.19	2.00	1503	1.08	1020	21.3	11.6
16	70	3.67	3.49	1503	1.08	1020	21.3	11.6
17	70	6.63	6.44	1503	1.08	1020	21.3	11.6
18	70	10.3	10.13	1503	1.08	1020	21.3	11.6
19	70	0.75	0.55	1874	1.14	1066	22.2	12.2
20	96.8	0.61	0.46	588	0.86	1087	20.0	10.6
21	96.8	0.66	0.50	843	0.94	1176	21.5	11.4
22	96.8	0.70	0.53	1141	1.01	1252	22.9	12.1
23	96.8	0.80	0.61	1874	1.14	1430	25.8	13.5

TABLE 2. Experimental conditions for sensor data in §5

very strong effects on the heat transfer mechanisms, are discussed in §6. Section 7 considers transient transition in detail. Finally, in §8, the transient response mechanisms are summarized. Methods of analysis for some of the effects found are also considered.

5. Sensor measurements of transient response

The regime diagram, figure 4, shows many distinct response mechanisms. The programme of local velocity and temperature measurements in the water studied these mechanisms in more detail. The measured transient velocity and temperature responses at different locations in the convection region are plotted as a function of time in the forms given in (7)–(10) below. For negligible relative surface thermal capacity, that is $Q^* \ll 1$, the one-dimensional transient response, given by Goldstein & Briggs (1964), is

$$\frac{t-t_\infty}{2q''_\infty \alpha^{\frac{1}{2}}/k} = \{i \operatorname{erfc} \xi\}\, \bar{\tau}^{\frac{1}{2}} \tag{7}$$

and

$$\frac{u}{8g\beta q''_\infty \alpha^{\frac{1}{2}}/k(1-Pr)} = \bar{\tau}^{\frac{3}{2}}\left(i^3 \operatorname{erfc}\xi - i^3 \operatorname{erfc}\frac{\xi}{Pr^{\frac{1}{2}}}\right); \quad Pr \neq 1, \tag{8}$$

where $\xi = y/2(\alpha\bar{\tau})^{\frac{1}{2}}$ and $i^n \operatorname{erfc}\xi$ is the nth integral of $\operatorname{erfc}\xi$. Including a thermal capacity c'' per unit area, Goldstein & Briggs (1964), gave

$$\frac{t-t_\infty}{q''_\infty \alpha^{\frac{1}{2}}/k} = \frac{1}{a}\left[2a\frac{\bar{\tau}^{\frac{1}{2}}\,\mathrm{e}^{-\xi^2}}{\pi^{\frac{1}{2}}} - 2a\bar{\tau}^{\frac{1}{2}}\xi \operatorname{erfc}\xi + \exp\left(2a\bar{\tau}^{\frac{1}{2}}\xi + a^2\bar{\tau}\right)\operatorname{erfc}\left(\xi + a\bar{\tau}^{\frac{1}{2}}\right) - \operatorname{erfc}\xi\right] \tag{9}$$

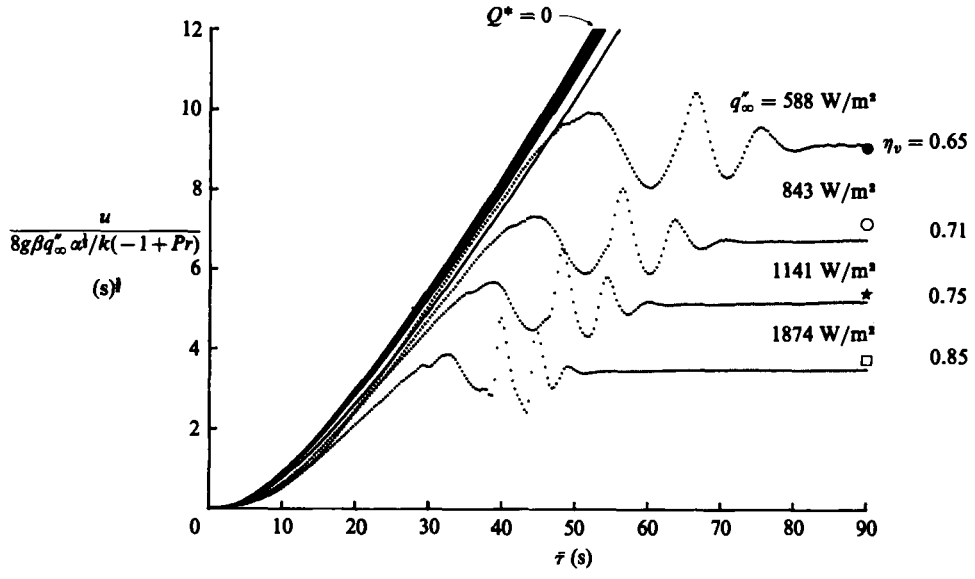

FIGURE 5. Transient velocity response for various q''_∞, at $x = 0.29$ m. The short-time solutions with and without the effects of surface thermal capacity are contained within two separate bands. The non-dimensional normal distance variable $\eta = yG^*/5x$ is shown for each curve. Symbols at the right show the laminar-boundary-layer predictions at $Pr = 6.2$.

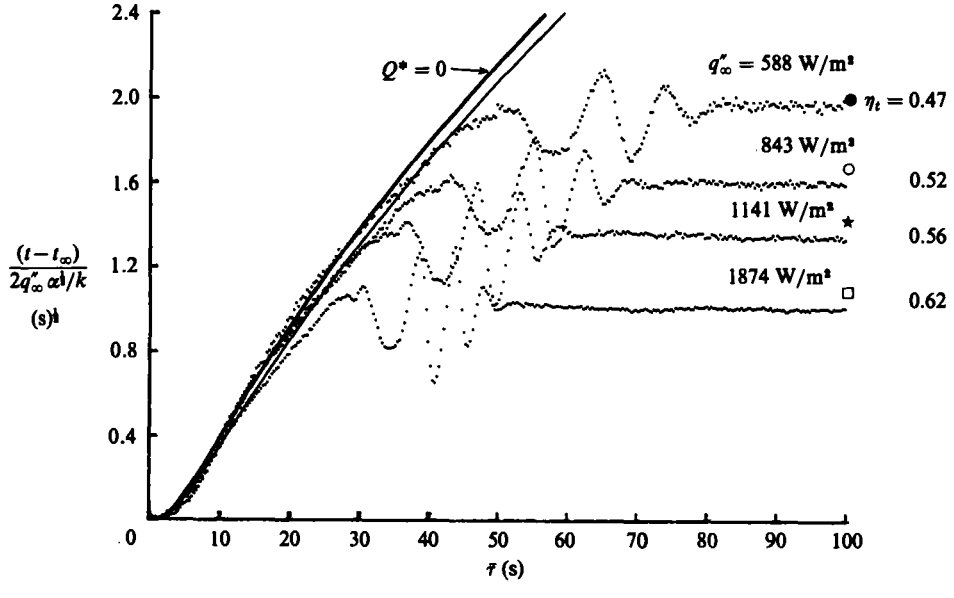

FIGURE 6. Transient temperature response for various q''_∞, at $x = 0.29$ m. The short-time solutions, with and without the effects of surface thermal capacity are shown as solid curves. The non-dimensional distance variable is shown for each curve. Symbols at the right show the laminar-boundary-layer predictions at $Pr = 6.2$.

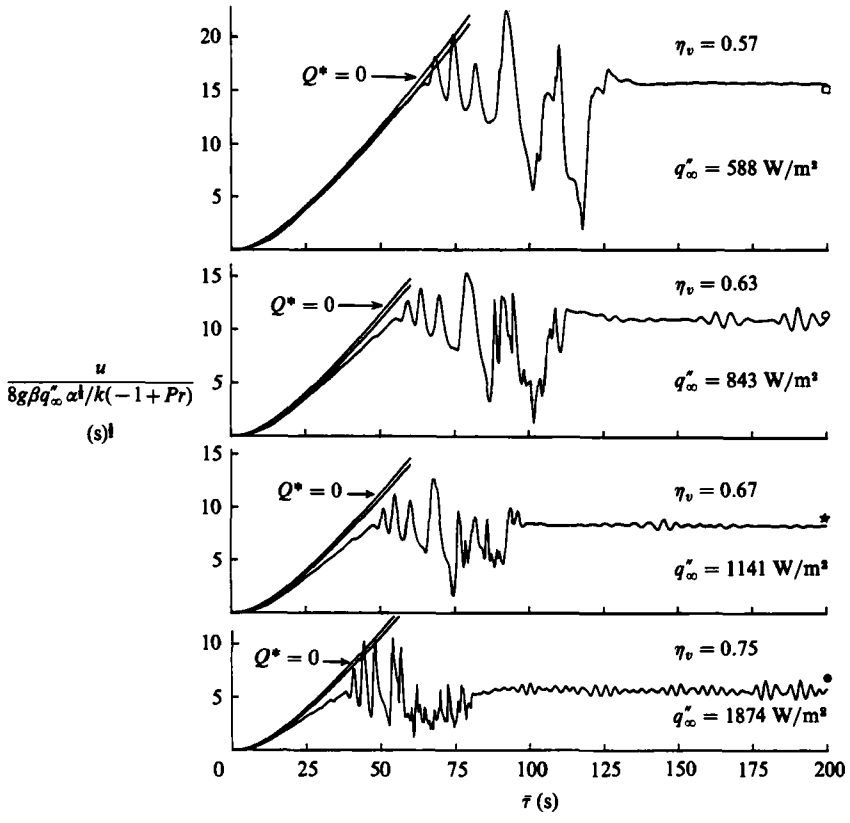

FIGURE 7. Transient velocity response for various q''_∞, at $x = 0.7$ m. The short-time solutions, with and without the effects of surface thermal capacity are shown. Symbols at the right correspond to the steady laminar-boundary-layer calculations at $Pr = 6.2$, at the indicated η_v.

and

$$\frac{u}{g\beta q''_\infty \alpha^{\frac{1}{2}}/k(1-Pr)} = \Bigg[8\left(i^3 \operatorname{erfc}\xi - i^3 \operatorname{erfc}\frac{\xi}{Pr^{\frac{1}{2}}}\right) + \frac{1}{a^3\bar{\tau}^{\frac{3}{2}}}\{\exp(a^2\bar{\tau} + 2a\bar{\tau}^{\frac{1}{2}}\xi)\operatorname{erfc}(\xi + a\bar{\tau}^{\frac{1}{2}}) - \exp(a^2\bar{\tau} + 2a\bar{\tau}^{\frac{1}{2}}\xi/Pr^{\frac{1}{2}})\operatorname{erfc}(\xi/Pr^{\frac{1}{2}} + a\bar{\tau}^{\frac{1}{2}})\} - \frac{1}{a^3\bar{\tau}^{\frac{3}{2}}}\left\{\sum_{r=0}^{2}(-2a\bar{\tau}^{\frac{1}{2}})^r i^r \operatorname{erfc}\xi - \sum_{r=0}^{2}(-2a\bar{\tau}^{\frac{1}{2}})^r i^r \operatorname{erfc}\frac{\xi}{Pr^{\frac{1}{2}}}\right\}\Bigg]\bar{\tau}^{\frac{3}{2}} \quad \text{for } Pr \neq 1, \tag{10}$$

where $a^2 = (\rho c_p k)/(c'')^2$.

These relations apply for constant fluid properties. The greatest variations in the experiments were in the kinematic viscosity ν, the largest being about 11%. In reducing the data, fluid properties were evaluated at the local film temperature in steady state, $\frac{1}{2}(t_0 + t_\infty)$.

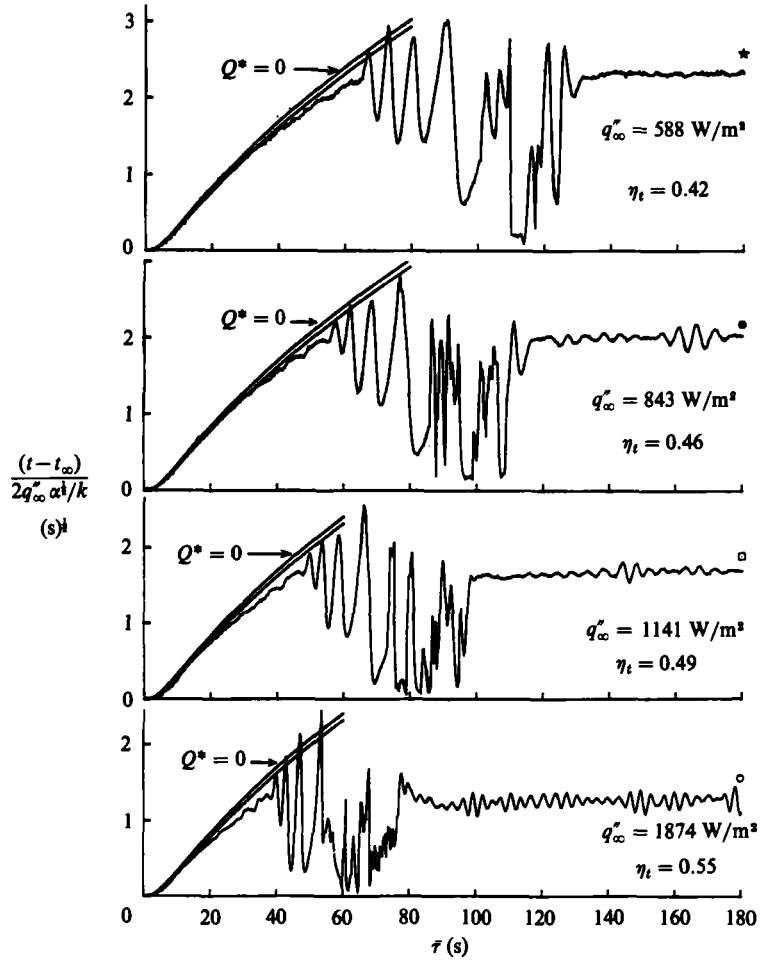

FIGURE 8. Transient temperature response for various q''_∞, at $x = 0.7$ m. The short-time solutions, with and without the effects of surface thermal capacity are shown. Symbols at the right correspond to steady laminar-boundary-layer calculations at $Pr = 6.2$, at the indicated η_t.

5.1. *Transient velocity and temperature profiles*

The one-dimensional solutions and actual sensor data are plotted in figures 5 and 6, for runs 1, 2, 3 and 9 in table 2. The two velocity solutions, (8) and (10), each fall within the two separate bands seen in figure 5. The bandwidth arises because of the variation in fluid properties at the different flux levels. The upper dark band is for $Q^* = 0$ and the lower white band includes the effect of the actual surface thermal capacity. Since the thermal diffusivity variation is much less, in comparison, (7) and (9), for $t-t_\infty$, become two curves in figure 6.

The local fluid velocity and temperature increase slower than that calculated for $Q^* = 0$. The calculations that account for $Q^* \neq 0$ are in much better agreement with the data. Immediately after the arrival of the leading-edge effect, or entrainment, an approximately sinusoidal disturbance passes, for all heat input levels. It passes more quickly at higher input q''_∞. However, the frequency and relative amplitude are greater.

The points at $\bar{\tau} = 90$ s were calculated from steady boundary-layer theory, for

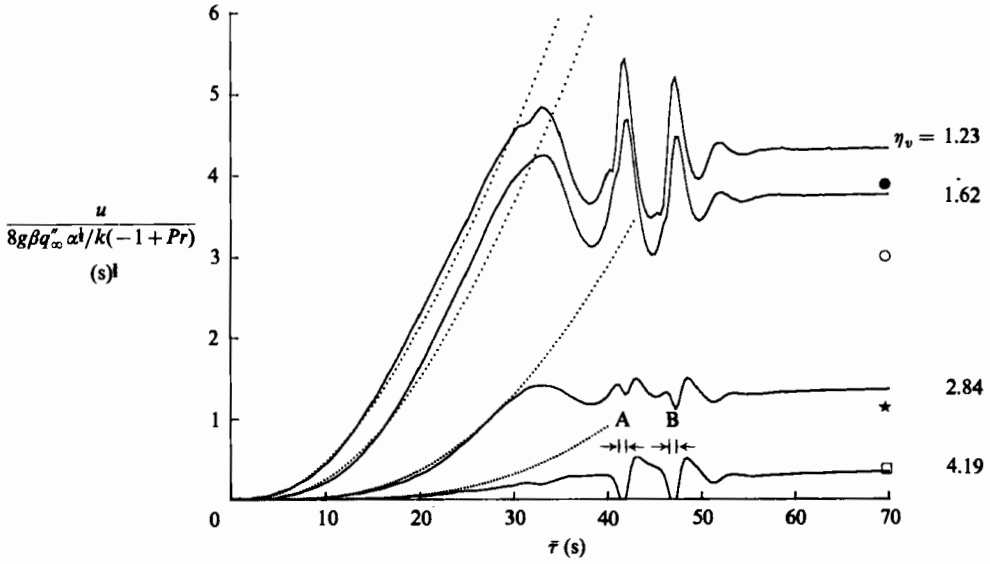

FIGURE 9. Transient velocity response further out from the surface, for $x = 0.29$ m and $q''_\infty = 1503$ W/m^2. Short-time solution with thermal capacity is shown. The non-dimensional distance variable is shown for each curve. Symbols at the right correspond to the steady, laminar-boundary-layer prediction.

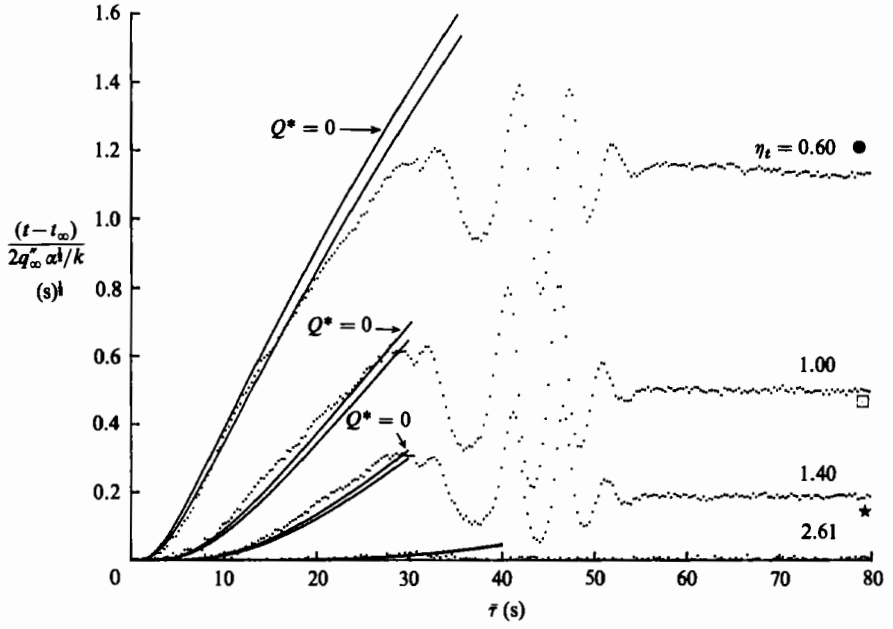

FIGURE 10. Transient temperature response further out from the surface, for $x = 0.29$ m and $q''_\infty = 1503$ W/m^2. Short-time solutions with and without thermal capacity are shown. The non-dimensional distance variable is shown for each curve. Symbols at the right correspond to the steady, laminar-boundary-layer prediction.

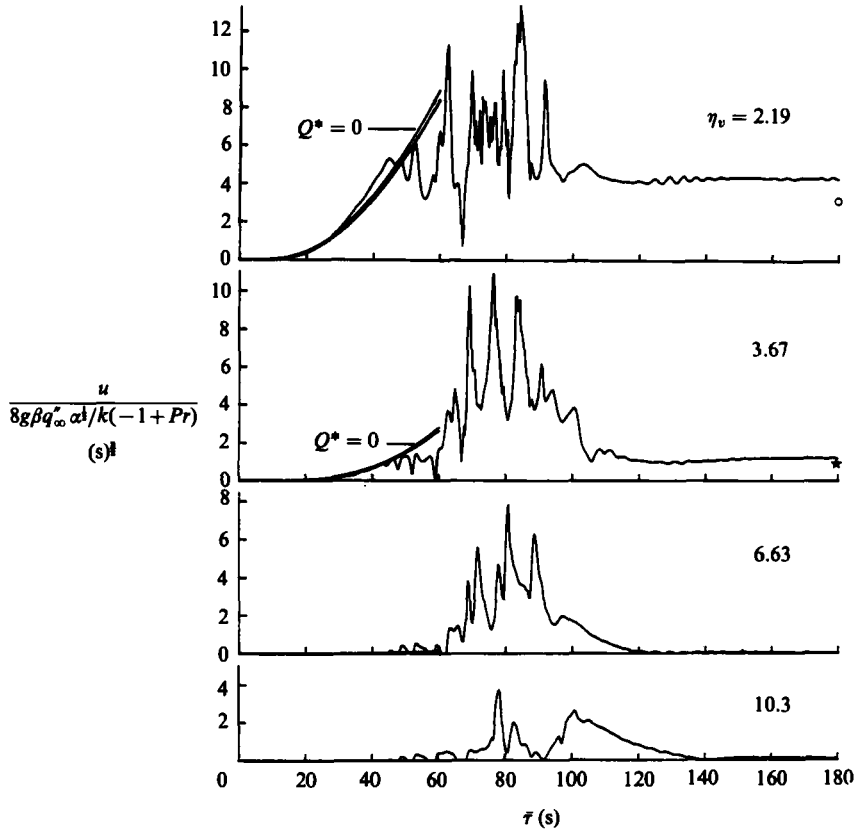

FIGURE 11. Transient velocity response further out from the surface, for $x = 0.7$ m and $q''_\infty = 1503$ W/m^2. Short-time solutions with and without thermal capacity are shown. The non-dimensional distance variable is shown for each curve. Symbols at the right correspond to the steady, laminar-boundary-layer prediction.

$Pr = 6.2$. The velocity data in figure 5 agree with these for $q''_\infty = 588$ W/m^2 but fall below for larger q''_∞, owing to the beginning of transition. The temperature data in figure 6 are within 5% of the laminar prediction, for $q''_\infty \leqslant 1141$ W/m^2. At $q''_\infty = 1874$ W/m^2 the disagreement is about 10%, owing, perhaps, to a larger property variation effect.

The very different velocity response for runs 10, 11, 12 and 19 is seen in figure 7. All short-time responses are terminated by one-dimensional transient transition. The early sinusoidal disturbances amplify and result in turbulent flow. This is followed by a return to transition flow, with small periodic disturbances. The corresponding temperature responses in figure 8 indicate that the mean temperatures during transient transition are far below the eventual steady mean temperatures. The flow visualizations in figure 3 (*b*) show a vigorous mixing of ambient fluid with the warmer fluid near the surface. The temporary decrease persists, until steady state is achieved.

5.2. *Transient response in the outer region*

Velocity and temperature results are seen in figures 9–12 for runs 5–8 and 15–18. Figures 9 and 10 apply to $x = 0.29$ m. The velocity levels in figure 9 at $\eta_v = y_v G^*/5x = 1.23$ and 1.62 exceed the laminar calculation, indicating velocity tran-

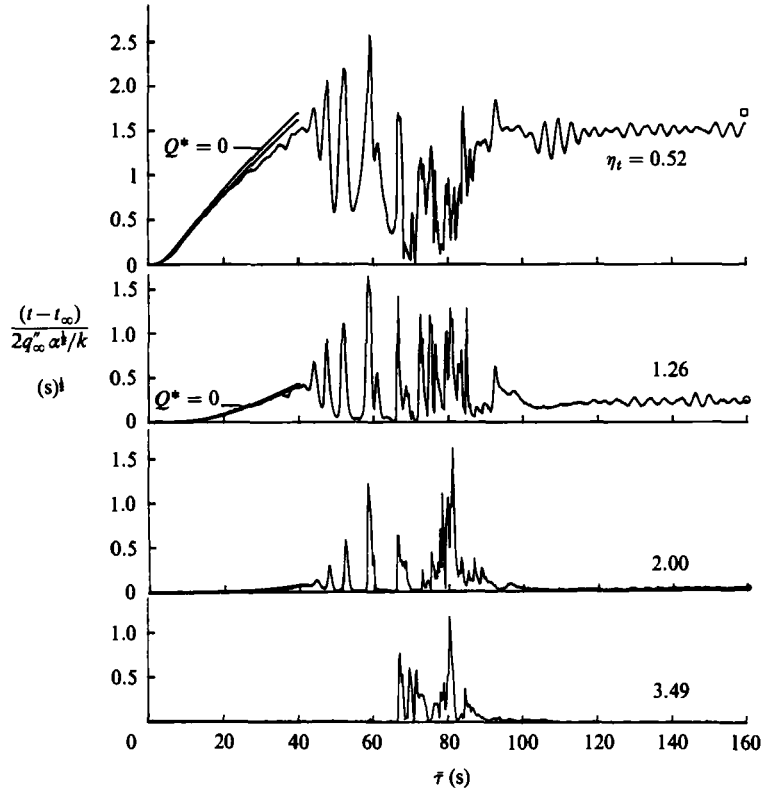

FIGURE 12. Transient temperature response further out from the surface, for $x = 0.7$ m and $q''_\infty = 1503$ W/m^2. Short-time solutions with and without thermal capacity are shown. The non-dimensional distance variable is shown for each curve. Symbols at the right correspond to the steady, laminar-boundary-layer prediction.

sition. Disturbance amplitude during the transient is much less at $\eta_v = 2.84$ and 4.19. At $\eta_v = 4.19$, during the periods shown as (A) and (B), there is no net upward local velocity. This is due to the strong inflow seen in the visualizations, during entrainment development in the outer boundary region. The eventual steady velocity is in good agreement with the laminar-boundary-layer theory. Outer regions of the velocity boundary region are apparently undistorted, for the relatively low $E = 15.0$.

The temperature data, at $x = 0.29$ m, in figure 10 indicate an overshoot during the one-dimensional transient, at all outer locations, beyond $\eta_t = 0.60$. A direct consequence of this is an overshoot in the thermal-boundary-region thickness, as reported by Goldstein (1959).

It is clear, in comparing figures 9 and 10, that the transient temperature disturbances are confined well within the velocity layer. The thermal region is much thinner in water.

The profiles further downstream at $x = 0.7$ m are seen in figures 11 and 12. Outside the eventual steady velocity maximum, at $\eta_v = 2.19$, an overshoot occurs. This suggests that the redistribution of momentum away from the velocity maximum, caused by velocity transition, starts during the transient itself. At larger distances out, some of the higher-frequency disturbance components disappear. Disturbance levels during the transient remain large even at $\eta_v = 10.3$. There, the steady velocity is only about 3 % of the maximum across the layer.

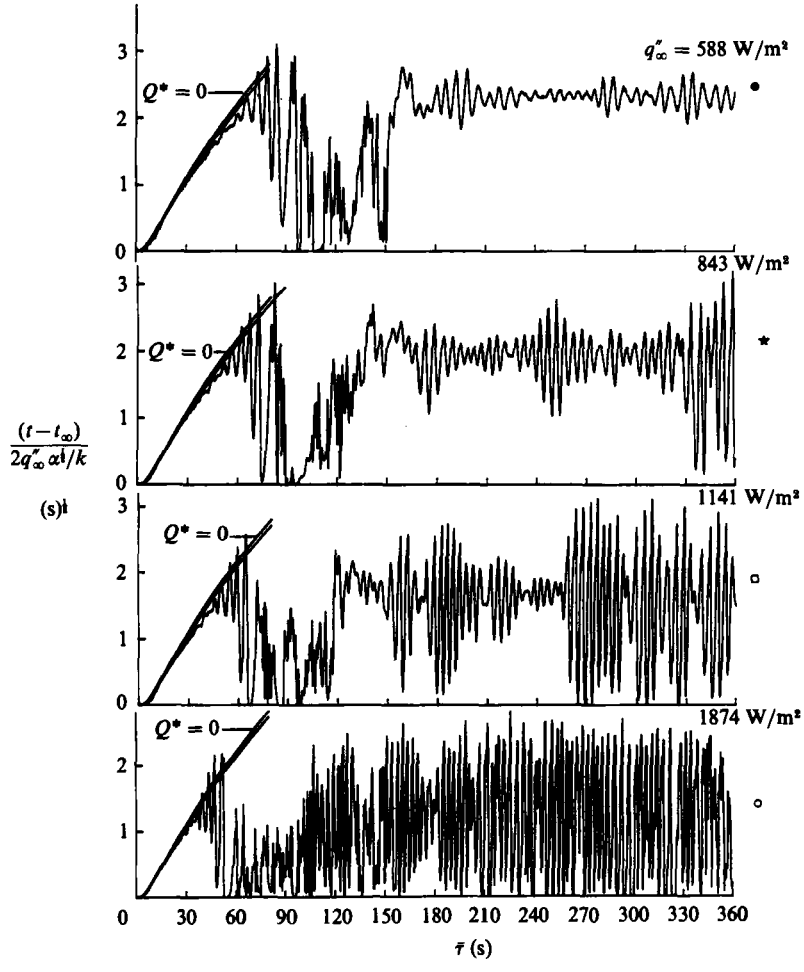

FIGURE 13. Development of turbulence with increasing q''_∞ at $x = 0.968$ m. Short-time solutions with and without surface thermal capacity effects are shown. Symbols at the right correspond to steady laminar-boundary-layer calculations at $Pr = 6.2$; ●, $\eta_t = 0.46$; ★, 0.50; □, 0.53; ○, 0.61.

The temperature distribution at $x = 0.7$ m, in figure 12 at $\eta_t = 0.52$, indicates a large decrease in the mean temperature from the final steady state, due to mixing with colder outer fluid. However, for larger η_t, the mean temperatures during transient transition actually exceed the final steady level. This arises from mixing with a thicker inner region at higher temperature. A transient overshoot in the thermal-layer thickness, similar to that in figure 10, is observed at $\eta_t = 2.00$.

Figures 11 and 12 clearly show that the region of transient transition, at $x = 0.7$ m, extends well beyond the thickness of the eventual steady boundary region. This is also confirmed by the visualization in figure 3. Figures 9 to 12 clarify the change in transport development downstream. These measurements relate to various stages of transition in steady state. Development of turbulence further downstream is discussed next.

5.3. *Development of turbulence in steady flow*

Disturbance amplitudes continue to increase as transition progresses. Also, disturbance energy is distributed toward smaller lengthscales. These aspects have been investigated in detail for steady mean flows as summarized in Gebhart & Mahajan (1982). Turbulence development during transient response is seen next, resulting from increased levels of thermal input.

Temperature response is seen in figure 13 for runs 20–23 at $x = 0.968$ m. Velocity data are similar and are not shown. For $q''_\infty = 588$ W/m^2, disturbance amplitude sharply decreases after $\bar{\tau} = 160$ s. Steady transition later arises. The disturbance amplitude in steady state is only about 10% of the mean. For $q''_\infty = 843$ W/m^2, the disturbance amplitude in steady flow is much higher. Also, large bursts occur more frequently and with longer durations. For $q''_\infty = 1141$ W/m^2, the burst amplitudes become even larger than the disturbance levels during the transient. For the highest flux, 1874 W/m^2, turbulence occurs during the transient and persists for all later times. The time required to achieve steady conditions is no longer as sharply defined as at the lower heating rates. The amplitude of temperature disturbances in steady state is about 80% of the mean. This is comparable with that observed by Jaluria & Gebhart (1974) at the end of transition.

6. Transient surface-temperature measurements

The thermocouples embedded in the surface structure determined its transient temperature response. Thereby, the transient heat-transfer characteristics are known. Several unexpected effects were found. Experiments by Goldstein (1959) and by Sammakia *et al.* (1982), in water, were for conditions for which $Gr_x^* < 10^9$. A one-dimensional response was found until the local instantaneous temperature increased to the steady laminar asymptotic value. Laminar-boundary-layer analysis was then accurate for all later times. Our results show that for more vigorous flows in the range $10^{10} < Gr_x^* < 5 \times 10^{12}$, a significant overshoot in the heat-transfer coefficient occurs during transient transition. Surface-temperature response and heat-transfer results for these conditions are shown in figures 14–16.

Figure 14 shows the surface-temperature response at various heating rates, at $x = 43.5$ cm. Also shown there are the one-dimensional solutions both for $Q^* = 0$ and $Q^* > 0$. For $q''_\infty = 372$ W/m^2, the departure from the conduction solution quickly becomes steady state. For $q''_\infty = 843$ W/m^2, the temperature rises nearly to the boundary-layer asymptote, then drops and becomes the steady value, at about $\bar{\tau} = 85$ s. As q''_∞ is increased further, the drop in surface temperature, late during the transient, becomes increasingly larger.

The conduction transient instantaneous heat transfer coefficient, for $Q^* = 0$, is calculated from

$$h(x, \bar{\tau}) = \frac{q''_\infty}{t_0 - t_\infty}, \tag{11}$$

where $(t_0 - t_\infty)$ is given by (7). For $Q^* \neq 0$, from (9)

$$h(x, \bar{\tau}) = \frac{q''_\infty [1 - \operatorname{erfc}(a\bar{\tau})^{\frac{1}{2}} \, e^{a^2 \bar{\tau}}]}{t_0 - t_\infty}. \tag{12}$$

The decrease of surface-temperature levels, which occurs during the transient, leads to an increase in the actual instantaneous local heat-transfer coefficient $h(x, \bar{\tau})$.

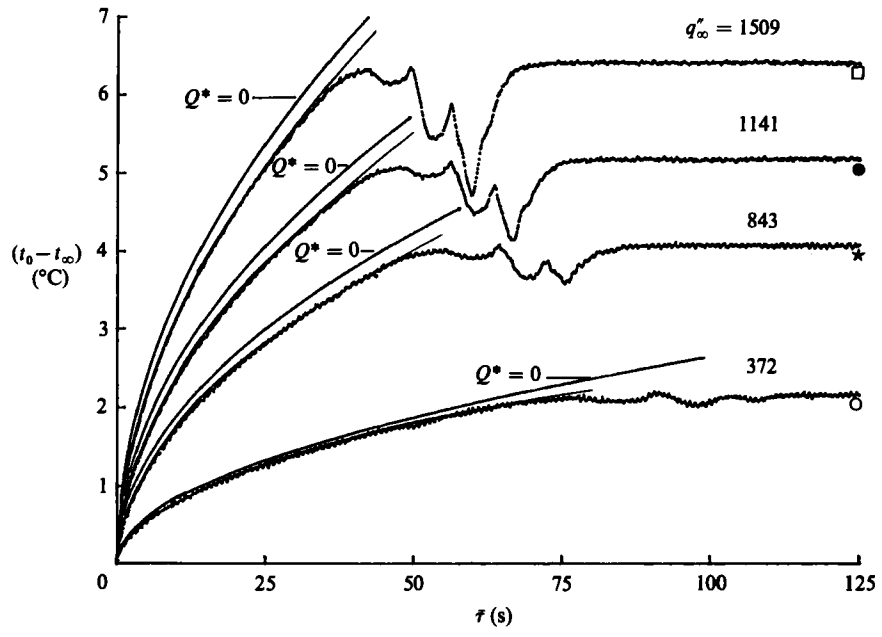

FIGURE 14. Surface-temperature response for various q''_∞ at $x = 0.435$ m. Solid lines correspond to short-time solutions with and without thermal capacity. Symbols at the right are laminar-boundary-layer predictions at $Pr = 6.0$.

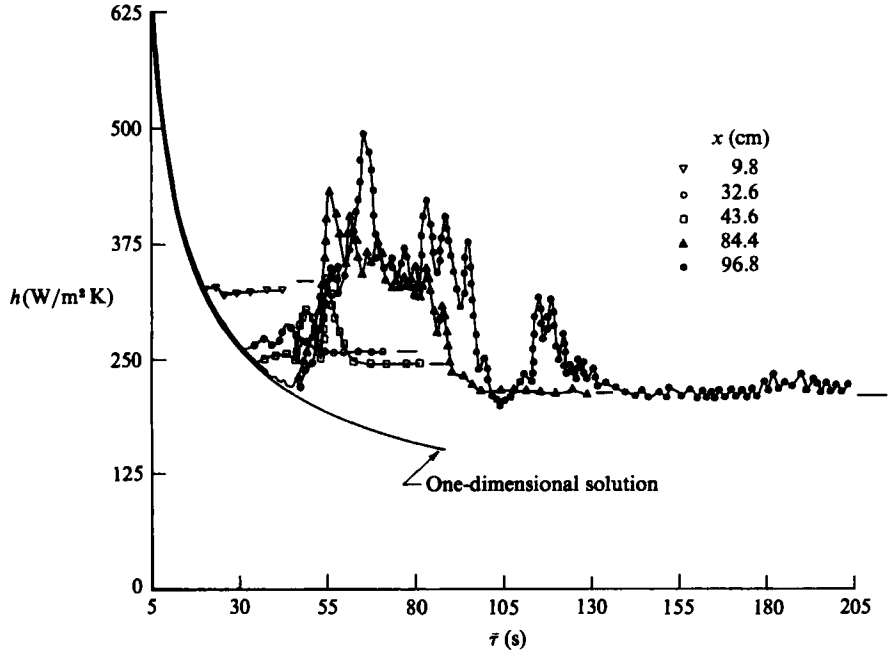

FIGURE 15. Instantaneous local heat-transfer coefficient at various x for $q''_\infty = 1874$ W/m². One-dimensional predictions with and without surface thermal capacity are indistinguishable on the plot. Horizontal lines at the right are laminar-boundary-layer predictions for $Pr = 6.0$.

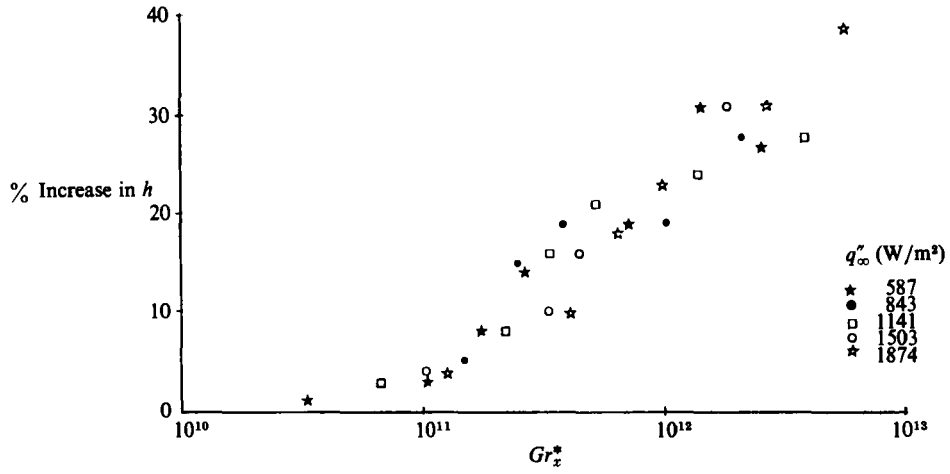

FIGURE 16. Average increase in local heat-transfer coefficient during the transient over the steady value.

Figure 15 shows this effect for $q''_\infty = 1874$ W/m², at various downstream locations. At $x = 9.8$ cm, steady state is achieved shortly after deviation from the one-dimensional transient. At $x = 32.6$ cm, there is an increase in $h(x, \bar{\tau})$ of about 10%, over the steady value. At yet larger distances, the increase becomes larger and persists longer.

The eventual steady value at $x = 84.4$ cm is seen to be in good agreement with the laminar-boundary-layer prediction shown, even though $E = 24.5$ there. This is well beyond the beginning of transition in steady flow, as seen from local sensor measurements in §5. Similar behaviour was observed by Vliet & Liu (1969) and Qureshi & Gebhart (1978). The surface thermal capacity apparently damps out small flow disturbances. In figure 15, the decrease in mean steady surface temperature, from the laminar trend, does not begin until $E = 25.9$ at $x = 96.8$ cm.

These surface temperature data show that one-dimensional transport persists until the onset of transient transition. Also, for large times, steady-state values are achieved. In the intermediate range of time, the local heat-transfer coefficient exceeds its eventual asymptote. This increase, averaged over the transient transition period, is shown in figure 16 as a percentage of the steady value. The times for the appearance of first disturbances and for the establishment of steady state are discussed in §7. Local surface temperatures were averaged through the time in between these bounding values to obtain the average increase in the heat-transfer coefficient during the transient.

In figure 16, for $Gr_x^* < 3 \times 10^{10}$, the average transient increase in heat-transfer coefficient is negligible. It becomes significant at higher values of Gr_x^*, for all values of q''_∞ considered. For the highest value, $Gr_x^* = 5 \times 10^{12}$, the increase is about 40%. For $Gr_x^* > 5 \times 10^{12}$, the times of establishment of steady state are not clear, since transition during the transient becomes indistinguishable from steady transition. As seen in §5.3, local sensors show similar trends.

7. Transient transition

The departure from one-dimensional response depends both on q''_∞ and x, if purely laminar flow persists. However, it has been seen that other mechanisms sometimes intercede, in more vigorous flow circumstances. Other than developing entrainment, earliest events have included disturbances in local sensor outputs and disturbances in local surface temperature.

These matters are discussed in terms of a propagation plane, of downstream penetration x *vs.* time. Figure 17 compares the actual propagation of several flow features with a calculation based on the criterion of Brown & Riley (1973) for the leading-edge or entrainment effect, shown for $Q^* = 0$ and $Pr = 6.2$. The dotted lines, for $q''_\infty = 92$, 587 and 1142 W/m^2, are the entrainment development times seen in flow visualizations. These developments generally agree in trend with the calculations, but are faster. For $q''_\infty = 92$ W/m^2, the entrainment developed for $x < 100$ cm, before one-dimensional transient transition occurred. For the heating rates of 587 and 1142 W/m^2, flow development by the entrainment effect is terminated by transient transition.

The solid lines, for $q''_\infty = 588$, 843, 1141, 1503 and 1874 W/m^2, are the times for first disturbances, obtained from local sensor data. The data trends again initially agree with the calculation, although they are slightly higher. Downstream, the data depart from the theory at almost a single but different value of time for each q''_∞.

The dashed-dotted lines for $q''_\infty = 588$ and 1874 W/m^2 are the first disturbance times in the surface-temperature data. The trends are similar to those of the sensor data, but lag in time. This occurs because the smaller-amplitude disturbances are damped by the surface thermal capacity.

7.1. *Predictive parameters for transient transition*

The above results indicate that the several departures from the trend of leading-edge propagation rate occur at the same time, for each q''_∞. Analysis suggests $\tau = (g\beta q''_\infty/k)^{\frac{1}{2}}\overline{\tau}$ as the relevant non-dimensional time parameter, for one-dimensional transient response. The local sensor data of figure 17 are replotted in figure 18 as $X = (Gr^*_x)^{\frac{1}{4}}$ *vs.* τ, along with the calculation of Brown & Riley (1973). Agreement in trend is seen for $\tau < 85$. Thereafter, undisturbed one-dimensional flow does not persist anywhere along the surface. This indicates that transient transition of the one-dimensional flow occurs at an almost constant value of τ.

The instantaneous non-dimensional thermal energy flux of the one-dimensional flow is given by

$$E_{TT} = \int_0^\infty U(\xi,\tau)\,T(\xi,\tau)\,\mathrm{d}\xi, \tag{13}$$

where

$$U = \frac{u}{(\nu^2 g\beta q''_\infty/k)^{1/4}}, \quad T = \frac{t-t_\infty}{(\nu^2 q''^3_\infty/g\beta k^3)^{1/4}}.$$

The U and T profiles are well approximated by the $Q^* = 0$ forms, (7) and (8). Substituting these in (13) gives

$$E_{TT} = \frac{16\tau^2}{Pr(1-Pr)}\int_0^\infty F_1(\xi)\,F_2(\xi)\,\mathrm{d}\xi, \tag{14}$$

where

$$F_1(\xi) = i\,\mathrm{erfc}\,\xi, \quad F_2(\xi) = i^3\,\mathrm{erfc}\,\xi - i^3\,\mathrm{erf}\,(\xi/Pr^{\frac{1}{2}}).$$

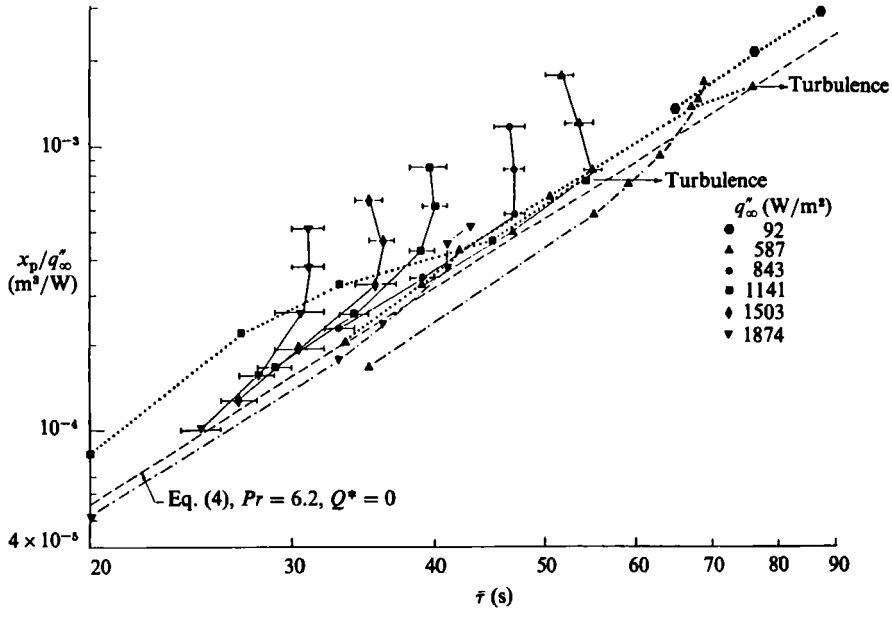

FIGURE 17. Termination of one-dimensional transport. Events plotted are: ·····, times for entrainment development from flow visualizations; ——, first disturbance times from local sensor data; –·–·–, first disturbances in surface-temperature data. Horizontal bars in local sensor data indicate differences in observed timings for thermal and velocity disturbances.

Thus, (14) yields a single value of E_{TT}, when disturbances were first seen. For $\tau = 85$ and $Pr = 6.2$ the numerical integration of right-hand side of (14) yields $E_{TT} = 19.7$. This, then, is the condition for transient transition.

7.2. *Transient disturbance frequencies*

Steady vertical natural-convection boundary-region flows are well known to selectively amplify a very narrow band of frequencies, from the spectrum of a naturally occurring disturbance. As summarized by Gebhart & Mahajan (1975), the experimental evidence is very strong that complicated disturbances are filtered downstream for an essentially single value of frequency. This is called the characteristic frequency. For a given flow condition, the generalized characteristic frequency depends only on the Prandtl number.

Disturbance frequencies were determined from the current data by a fast Fourier transform. Disturbance data and the discrete Fourier transforms are seen in figures 19 and 20, first during the transient and then in steady state, for $q''_\infty = 1874$ W/m² and at various x. The disturbances at the left in figure 19 are at five downstream locations. At $x = 0.19$ and 0.29 m they quickly damp out. For the other three downstream locations, the flow undergoes transition to turbulence later in the transient. Only the initial amplifying disturbances are plotted for these locations. The transforms on the right show that disturbance energy is concentrated in a narrow frequency range. Also, the principal frequency is seen to increase with x, by a factor of about two over this x-range.

Figure 20 shows sensor and transformed data in eventual steady flow, for the same q''_∞ as in figure 19. Disturbance amplitudes in steady flow first became measurable at $x = 0.49$ m. As seen in the transform, these are almost a single periodic variation.

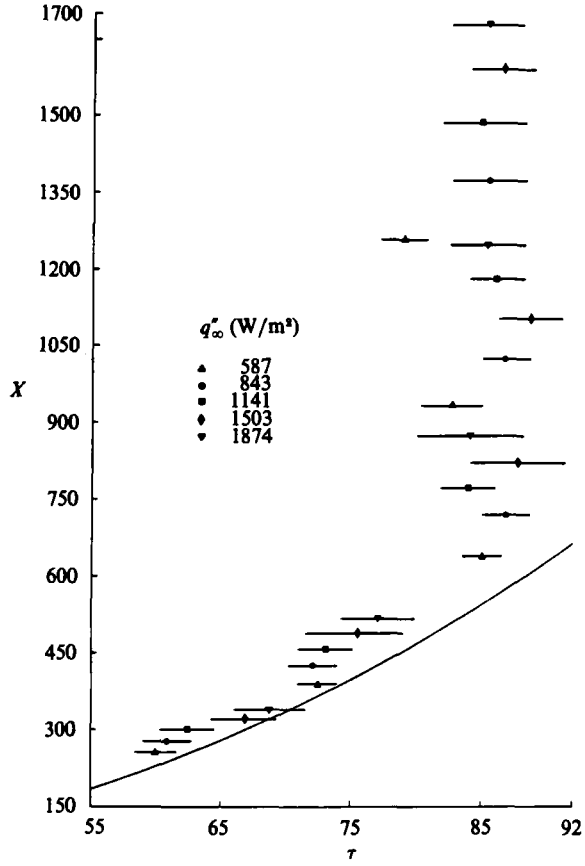

FIGURE 18. Non-dimensional times for the first observed disturbances in local sensor data, at various downstream locations. Horizontal bar with each data point shows the difference in observed time for velocity and temperature disturbance. The solid curve corresponds to the leading-edge-propagation estimate from Brown & Riley (1973) for $Pr = 6.2$ and $Q^* = 0$.

Further downstream, at $x = 0.7$ m, additional frequency components have appeared. Frequency broadening continues to $x = 0.968$ m, as the disturbance energy is further distributed.

The physical frequencies f, observed here, were normalized as in steady flows as $\Omega^* = 2\pi f[k/g\beta q''_\infty]^{\frac{1}{2}}$. The results are plotted in figure 21 on the (Ω^*, G^*)-plane for steady flow. Also shown, for $Pr = 6.7$, are the neutral stability and amplification contours for steady flow, from Hieber & Gebhart (1971), as reinterpreted by Gebhart & Mahajan (1982). The amplification contours represent $e^A = -\int_{\frac{1}{2}}^{1} \alpha_i \, dG^* =$ constant, where α_i is the downstream spatial amplification rate. The horizontal line, $\Omega^* = 0.675$, is the established characteristic frequency for $Pr = 6.7$.

Although the stability analysis for steady base flows is not directly applicable for the present transient results, the new frequency data, in largely laminar flows, shown as solid symbols, indicate a very conclusive trend. For $G^* < 700$, the data are below the $\Omega^* = 0.675$ line. However, for $G^* > 700$, they are very close to it. In the experiments reported here, naturally occurring disturbances in steady flow first became observable around $G^* = 700$. All such data are shown as open symbols in figure 21. They are also seen to be in excellent agreement with $\Omega^* = 0.675$.

Clearly, the same frequency filtering mechanism also is present in transients.

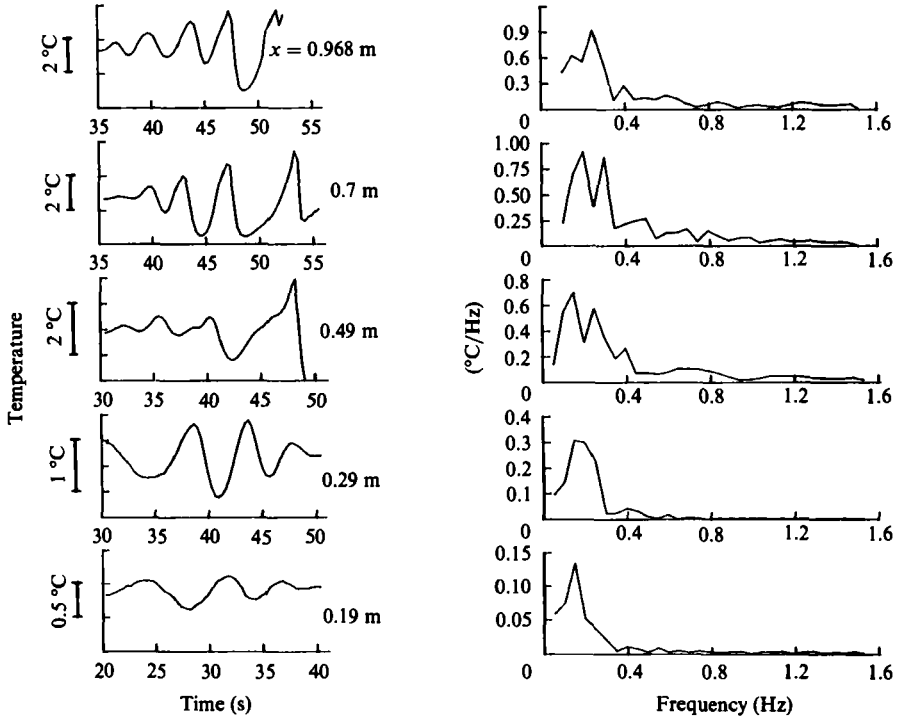

FIGURE 19. Temperature disturbances observed during the transient at various downstream locations, for $q''_\infty = 1874$ W/m². Curves at the left are time records of sensor data in the water. Corresponding discrete Fourier transforms are shown at the right.

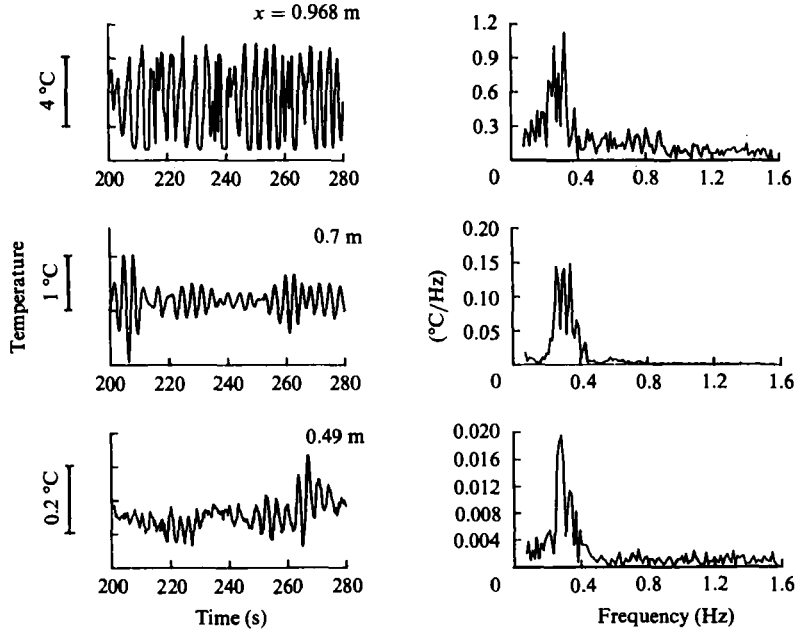

FIGURE 20. Temperature disturbances observed in steady data at various downstream locations, for $q''_\infty = 1874$ W/m². Curves at the left are time records of sensor data in water. Corresponding discrete Fourier transforms are shown at the right.

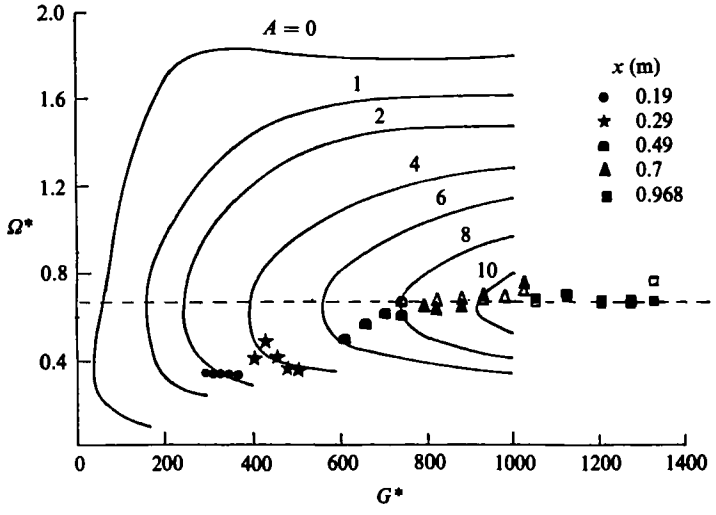

FIGURE 21. Observed frequencies of sinusoidal disturbances during the transient. Solid curves are constant-amplification contours for $Pr = 6.7$, for a steady base flow, vertical natural-convection boundary layer from Gebhart & Mahajan (1982). Unfilled symbols correspond to disturbances observed in the present data in the steady state.

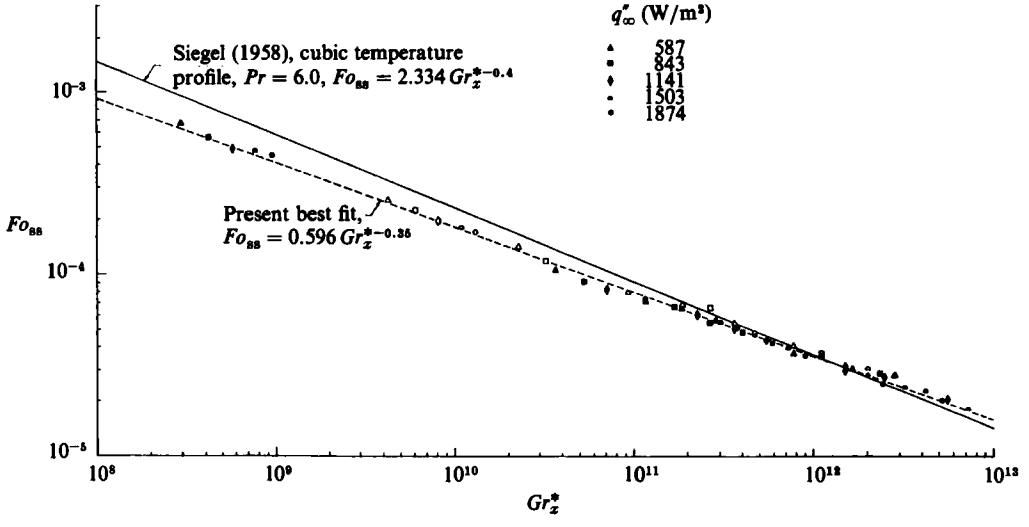

FIGURE 22. Steady-state achievement times for various Gr_x^*. The solid curve is the prediction from Siegel (1958). Dashed line corresponds to the best fit through present data. Unfilled symbols correspond to local sensor data and filled symbols to surface thermocouples.

Disturbance energy is again concentrated in a narrow frequency range. These disturbances amplify and cause transition during the transient.

As seen in the introduction to this section, the disturbances at short downstream distances correlate in trend with the leading-edge-effect propagation times. Their frequencies, to the left in figure 21, are less than $\Omega^* = 0.675$. The disturbances at higher G^* presumably result instead from the selective amplification of a preferred component of this leading-edge-effect disturbance. This conclusion is supported by the visualizations in figures 2 and 3.

Similar disturbance-frequency measurements in transients in air, by Mollendorf & Gebhart (1970) and Mahajan & Gebhart (1978), were also found to fall below the characteristic frequency path, in the range $300 < G^* < 1900$. In the light of the present result, it appears likely that these disturbances were also indirectly due to the leading-edge-effect disturbance. We recall that natural-convection flow velocities are about an order-of-magnitude faster in air, for comparable heating conditions. Therefore, the leading-edge effect may sweep the entire surface, before any instabilities grow in the one-dimensional transient.

7.3. *Times to steady flow*

In order to interpret transient effects and also to best use the transport data available for steady flows, it is necessary to know the transient time to steady state. Previous experimental studies have not indicated a correlation of such times $\bar{\tau}_s$. A correlation is given in figure 22, in terms of $Fo_{ss} = \alpha\bar{\tau}_s/x^2$, as a function of Gr_x^*. Data are shown from both local sensors (filled symbols) and surface-temperature thermocouples (open symbols). The solid line is the prediction of the analysis of Siegel (1958). The new data also indicate a linear trend. However, the slope is different. The analysis used integral forms of the boundary-layer equations. Also, the flow was assumed to remain laminar. Experimental studies have indicated that many other mechanisms commonly arise. The linear best fit through the new data, the dashed line in figure 22, is

$$Fo_{ss} = 0.596(Gr_x^*)^{-0.35}, \quad \text{for } 3\times10^8 < Gr_x^* < 7\times10^{12} \tag{15}$$

8. Conclusions

Experimental investigation of transient natural-convection response adjacent to a tall vertical surface has clarified the mechanisms of flow development, starting from quiescence to a steady downstream-developing boundary layer. Flow and transport evolution depend very strongly on input flux and downstream location.

Two different instability mechanisms are inferred from our experiments. After the development of entrainment, as in figure 2, instabilities appear to arise primarily from motion pressure effects. An oscillation in motion pressure, around the steady average level, may result from an initial transient overshoot of the flow entrainment rate. This is consistent with the transient overshoot in the velocity component u, see figure 5. These pressure oscillations around the eventual mean value are likely to result in alternate entrainment and detrainment. This was observed as counterclockwise transient vortices, at various x-locations. Any analytical formulation of these mechanisms must retain the pressure effects during the transient.

The second instability mechanism arises at larger downstream distances. There, the one-dimensional transient flow may become unstable even before the entrainment development from the leading edge arrives. Past calculations concerning transient instability have followed one of three methods. The simplest uses a quasi-steady flow formulation. Disturbance growth is assumed if they grow faster than the base flow itself. Time then enters only as a parameter. Solutions are obtained using standard linear stability techniques. This method is applicable only to slowly time-varying base flows. It has been shown to be inaccurate for impulsively started flows (Shen 1961).

The second approach treats the initial-value problem. It considers the time evolution of the base flow, along with superimposed small disturbances of various spatial forms. Random initial conditions may be supplied to the equations governing

the temporal growth of small disturbances. The governing equations for both the base flow and disturbances are then integrated forward in time. The base flow is termed unstable if the disturbance kinetic energy grows at a faster rate than that of the base flow.

The limitation to small disturbances of a given spatial form is avoided in the third approach. It employs the energy instability formulation. A positive definite energy functional is formed for the disturbance energy. Sufficient conditions for the exponential decay of this functional with time are then investigated, to obtain onset times for disturbances of arbitrary initial amplitude. Results of this method applied to suddenly heated or cooled horizontal fluid layers are discussed by Homsy (1973).

Extensions of the last two methods appear to be promising for analysing the transient instabilities seen in these one-dimensional flows. The transient-disturbance-frequency data and the time of the appearance of first disturbances provide a starting point for such studies.

The authors acknowledge the support through National Science Foundation grant CBT 84 18517 in this research. They also thank Dr B. Sammakia for many helpful discussions during the experimental program. Y. J. was partially supported by the Naval Postgraduate School Research Foundation during the preparation of the final manuscript.

REFERENCES

BROWN, S. N. & RILEY, N. 1973 Flow past a suddenly heated vertical plate. *J. Fluid Mech.* **59**, 225.

CALLAHAN, G. D. & MARNER, W. J. 1976 Transient free convection with mass transfer on an isothermal vertical flat plate. *Intl J. Heat Mass Transfer* **19**, 165.

CAREY, V. P. & GEBHART, B. 1981 Visualization of the flow adjacent to a vertical ice surface melting in cold pure water. *J. Fluid Mech.* **107**, 37.

GEBHART, B. 1961 Transient natural convection from vertical elements. *Trans. ASME* C: *J. Heat Transfer* **83**, 61.

GEBHART, B. 1971 Transient flows, effects of unsteady surface conditions on stability, and flow separation in buoyancy induced flows. In *IUTAM Symp. on Recent Research on Unsteady Boundary Layers, Québec,* p. 513.

GEBHART, B. & ADAMS, D. E. 1963 Measurements of transient natural convection on flat vertical surfaces. *Trans. ASME* C: *J. Heat Transfer* **85**, 25.

GEBHART, B. & DRING, R. P. 1967 The leading edge effect in transient natural convection flow from a vertical plate. *Trans. ASME* C: *J. Heat Transfer* **89**, 24.

GEBHART, B., DRING, R. P. & POLYMEROPOULOS, C. E. 1967 Natural convection from vertical surfaces, the convection transient regime. *Trans. ASME* C: *J. Heat Transfer* **89**, 53.

GEBHART, B. & MAHAJAN, R. L. 1975 Characteristic disturbance frequency in vertical natural convection flow. *Intl J. Heat Mass Transfer* **18**, 1143.

GEBHART, B. & MAHAJAN, R. L. 1982 Instability and transition in buoyancy-induced flows. *Adv. Appl. Mech.* **22**, 231.

GOLDSTEIN, R. J. 1959 Interferometric study of the steady state and transient free convection thermal boundary layers in air and in water about a uniformly heated vertical flat plate. Ph.D. dissertation, University of Minnesota.

GOLDSTEIN, R. J. & BRIGGS, D. G. 1964 Transient free convection about vertical plates and cylinders. *Trans. ASME* C: *J. Heat Transfer* **86**, 490.

HELLUMS, J. D. & CHURCHILL, S. W. 1961 Transient and steady state, free and natural convection, numerical solutions. *Paper 118 presented at the Intl Heat Transfer Conf., Boulder, CO.*

HIEBER, C. A. & GEBHART, B. 1971 Stability of vertical natural convection boundary layers: some numerical solutions. *J. Fluid Mech.* **48**, 625.

HOMSY, G. M. 1973 Global stability of time-dependent flows: impulsively heated or cooled fluid layers. *J. Fluid Mech.* **60**, 129.

ILLINGWORTH, C. R. 1950 Unsteady laminar flow of gas near an infinite flat plate. *Proc. Camb. Phil. Soc.* **46**, 603.

INGHAM, D. B. 1978*a* Transient free convection on an isothermal vertical flat plate. *Intl J. Heat Mass Transfer* **21**, 67.

INGHAM, D. B. 1978*b* Numerical results for flow past a suddenly heated vertical plate. *Phys. Fluids* **21**, 1981.

JALURIA, Y. & GEBHART, B. 1974 On transition mechanisms in vertical natural convection flow. *J. Fluid Mech.* **66**, 309.

JOSHI, Y. 1984 Transient natural convection flows in room temperature and cold water and natural and mixed convection flows in porous media. Ph.D. thesis, University of Pennsylvania.

KLEI, H. E. 1957 A study of unsteady state natural convection for a vertical plate. B.S. thesis, Massachusetts Inst. of Technology.

LURIE, H. & JOHNSON, H. A. 1962 Transient pool boiling of water on a vertical surface with a step in heat generation. *Trans. ASME* C: *J. Heat Transfer* **84**, 217.

MAHAJAN, R. L. & GEBHART, B. 1978 Leading edge effects in transient natural convection flow adjacent to a vertical surface. *Trans. ASME* C: *J. Heat Transfer* **100**, 731.

MAHAJAN, R. L. & GEBHART, B. 1979 An experimental determination of transition limits in a vertical natural convection flow adjacent to a surface. *J. Fluid Mech.* **91**, 131.

MARTIN, J. H. 1961 An experimental study of unsteady state natural convection from vertical plates. M.S. thesis, Cornell University.

MENOLD, E. R. & YANG, K.-T. 1962 Asymptotic solutions for unsteady laminar free convection on a vertical plate. *Trans. ASME* E: *J. Appl. Mech.* **84**, 124.

MOLLENDORF, J. C. & GEBHART, B. 1970 An experimental study of vigorous transient natural convection. *Trans. ASME* C: *J. Heat Transfer* **92**, 628.

QURESHI, Z. H. & GEBHART, B. 1978 Transition and transport in a buoyancy driven flow in water adjacent to a vertical uniform flux surface. *Intl J. Heat Mass Transfer* **21**, 1467.

RAJAN, V. S. V. & PICOT, J. J. C. 1971 Experimental study of the laminar free convection from a vertical plate. *Ind. Engng Chem. Fundam.* **10**, 132.

SAMMAKIA, B. & GEBHART, B. 1978 Transient and steady-state numerical solutions in natural convection. *Numer. Heat Transfer* **1**, 529.

SAMMAKIA, B. & GEBHART, B. 1981 Transient natural convection adjacent to a vertical flat surface: The thermal capacity effect. *Numer. Heat Transfer* **4**, 331.

SAMMAKIA, B., GEBHART, B. & QURESHI, Z. H. 1980 Measurements and calculations of transient natural convection in air. *Intl J. Heat Mass Transfer* **23**, 571.

SAMMAKIA, B., GEBHART, B. & QURESHI, Z. H. 1982 Measurements and calculations of transient natural convection in water. *Trans. ASME* C: *J. Heat Transfer* **104**, 644.

SHAUKATULLAH, H. 1977 An experimental investigation of the natural convection boundary layer over a uniform flux inclined surface. Ph.D. thesis, Cornell University.

SCHETZ, J. A. & EICHORN, R. 1962 Unsteady natural convection in the vicinity of a doubly infinite vertical plate. *Trans. ASME* C: *J. Heat Transfer* **84**, 334.

SHEN, S. F. 1961 Some considerations on the laminar stability of time-dependent basic flows. *J. Aero. Sci.* **28**, 397.

SIEGEL, R. 1958 Transient free convection from a vertical flat plate. *Trans. ASME* C: *J. Heat Transfer* **80**, 347.

SUGAWARA, S. & MICHIYOSHI, I. 1951 The heat transfer by natural convection in the unsteady state on a vertical flat wall. *Proc. First Japan Natl Cong. for Appl. Mech.*

VLIET, G. C. & LIU, C. K. 1969 An experimental study of turbulent natural convection boundary layers. *Trans. ASME* C: *J. Heat Transfer* **91**, 517.

YANG, K.-T. 1960 Possible similarity solutions for laminar free convection on vertical plates and cylinders. *Trans. ASME* E: *J. Appl. Mech.* **82**, 230.